Applied Catalysis B: Environmental 330 (2023) 122555

Contents lists available at ScienceDirect

Applied Catalysis B: Environmental

journal homepage: www.elsevier.com/locate/apcatb

Cobalt–aluminum oxide clusters-embedded γ-Al_2O_3 nanosheets for peroxymonosulfate activation: Interfacial pH-buffering property to eliminate cobalt leaching and boost the catalytic activity

Ding Liu, Zhenkun Su, Bo Han, Kaisheng Xia, Chenggang Zhou, Qiang Gao *

Faculty of Materials Science and Chemistry, China University of Geosciences, Wuhan 430078, China

ARTICLE INFO

Keywords:
Heterogeneous cobalt-based catalysts
Peroxymonosulfate
Interfacial pH buffering property
No cobalt leaching
High catalytic activity

ABSTRACT

Cobalt–aluminum oxide clusters-embedded γ-Al_2O_3 nanosheets (CAO@AO) were facilely fabricated and developed for peroxymonosulfate (PMS) activation. Interestingly, the Al–OH-rich amphiphilic surface of CAO@AO endowed the catalyst with unique interfacial pH-buffering property, which stabilized the reaction media at nearly neural level and thus prevented the cobalt sites from leaching. Moreover, the presence of Al–OH groups around the Co−Al oxide clusters facilitated the activation of PMS and the redox cycle of Co^{2+}/Co^{3+}, which resulted in a boosted catalytic activity. Consequently, the CAO@AO exhibited zero leaching of cobalt and high efficacy for PMS activation, enabling complete and ultrafast removal of metronidazole with a significantly higher turnover frequency (TOF, 1.83 min^{-1}) than that of Co_3O_4 (0.004 min^{-1}). It was also demonstrated that introducing suitable foreign metal into CAO@AO could further enhance the catalytic activity (e.g., TOF of Mn(40%)-CAO@AO: 5.80 min^{-1}). Furthermore, Mn(40%)-CAO@AO-decorated granular support was synthesized that dominated a continuous-flow degradation in column reaction system.

1. Introduction

Heterogeneous activation of peroxymonosulfate (PMS, $KHSO_5$) over solid cobalt-based catalysts for the generation of sulfate radicals ($SO_4^{-}\bullet$) is a topic of great scientific interest in recent years due to its great potential for refractory organic pollutant removal in water treatment field [1–4]. Numerous cobalt-containing materials have been investigated as catalyst candidates for activation of PMS, including pure cobalt oxides/hydroxides/phosphides, cobalt-bearing multimetal oxides, and porous substrate-supported cobalt-based composites [5–7]. However, PMS decomposition not only produces $SO_4^{-}\bullet$ but also releases H^+ ions into the reaction solution that readily attack the solid catalyst [6,8,9]. As a result, cobalt leaching can hardly be avoided, which will cause secondary pollution and poor catalytic durability, actually unsatisfying the demand of practical applications [10,11]. Therefore, besides pursuit of high catalytic activity, elimination or at least minimization of cobalt leaching has become an urgent and high-priority task in the development of eco-friendly and highly durable heterogeneous catalyst/PMS systems.

One currently popular approach for the controlling of cobalt leaching during the heterogenous activation of PMS is to improve the chemical stability of solid cobalt-based catalysts through rational design of their compositions. It has been demonstrated that coupling of Co with some certain metals through strong oxygen-bridge bonds (i.e., Co–O–M, M = Fe, Ti, Al, and etc.) or doping Co into suitable solid substrates is effective to inhibit leaching of cobalt sites from the resulting solid catalysts [12–16]. Moreover, in many cases, compositional design of catalysts has also proven beneficial in enhancement of the catalytic activity by virtue of synergetic activation, electron reconstruction, or substrate-promoting effect [17–19]. However, despite considerable progresses that have been made in the development of solid cobalt-based catalysts, it still fails to completely avoid cobalt leaching in the presence of PMS, especially for the catalytic oxidation systems with relatively high PMS dosages (≥ 1 mM), where the final pH values of reaction solutions are generally below 3.5 [20].

Alternatively, controlling the pH of the reaction medium by addition of alkaline or pH-buffering solution represents a simple yet effective strategy for suppressing cobalt leaching. In this regard, introduction of alkaline solution can neutralize H^+ ion and thus effectively prevents the leaching of cobalt, but it is at the expense of sharply declined degradation performance because PMS will be rapidly exhausted once it encounters even slightly excess OH^- ion ($HSO_5^- + 2OH^- \rightarrow 2SO_4^{2-} + H_2O +$

* Corresponding author.
E-mail address: gaoqiang@cug.edu.cn (Q. Gao).

https://doi.org/10.1016/j.apcatb.2023.122555
Received 2 January 2023; Received in revised form 18 February 2023; Accepted 1 March 2023
Available online 4 March 2023
0926-3373/© 2023 Elsevier B.V. All rights reserved.

O_2) [3,21,22]. In contrast, addition of neutral or nearly neutral phosphate buffer solution (PBS) or borate buffer solution (BBS) can be capable of not only terminating the H^+ attack but assuring high utilization rate of PMS. Indeed, there have been many successful instances where the solid cobalt-based catalyst-mediated PMS oxidation systems with PBS or BBS as pH stabilizer exhibit negligible cobalt leaching, satisfied catalytic durability, and high degradation performance [23–25]. However, in order to provide sufficient pH-buffering capacity, the concentrations of buffer species (e.g., phosphate and borate) are generally several hundred times higher than their maximum allowable limits set by the regulatory authority [26], which is actually impractical and cost-prohibitive for real applications. Therefore, for satisfying the security and long-term effectiveness of solid cobalt-based catalyst-mediated PMS oxidation systems, new strategies are urgently needed to suppress or even eliminate cobalt leaching in an environmentally friendly and sustainable manner.

In this work, we reported that cobalt leaching-free and highly active PMS activation system could be actualized by utilizing the cobalt–aluminum oxide clusters-embedded γ-Al_2O_3 nanosheets (CAO@AO) as catalysts that possessed a unique interfacial pH-buffering property. The synthesis of CAO@AO catalysts was rather simple and only involved a "hydrothermal–Co^{2+} adsorption–calcination" process. The strong interfacial pH-buffering property of CAO@AO was attributed to the favorable amphiphilic nature of the surface Al–OH groups [27], which could stabilize the solution pH at nearly neutral level and thus completely eliminated the cobalt leaching. Moreover, the Al–OH groups could facilitate the activation of PMS and the redox cycle of Co^{2+}/Co^{3+}, which resulted in a boosted catalytic activity. Relying on these advantageous features, the CAO@AO exhibited a superior catalytic efficiency and durability in metronidazole (MNZ) degradation in comparation with Co_3O_4 and various ever-reported solid cobalt-based catalysts. In order to further enhance the catalytic activity and advance the practical application of CAO@AO, composition tunning of active component, in situ immobilization on granular support, and continuous-flow degradation were also studied.

2. Experimental

2.1. Chemicals and raw material

Aluminum nitrate nonahydrate ($Al(NO_3)_3{\cdot}9\ H_2O$), potassium sulfate (K_2SO_4), urea ($CO(NH_2)_2$), cobalt acetate tetrahydrate ($Co(CH_3COO)_2{\cdot}4\ H_2O$), manganese acetate tetrahydrate ($Mn(CH_3COO)_2{\cdot}4\ H_2O$), iron acetate hydrate ($Fe(CH_3COO)_2OH{\cdot}nH_2O$), copper acetate monohydrate ($Cu(CH_3COO)_2{\cdot}H_2O$), anhydrous methanol (MeOH), metronidazole (MNZ, $C_6H_9N_3O_3$), methylene blue (MB, $C_{16}H_{18}ClN_3S$), ofloxacin (OFX, $C_{18}H_{20}FN_3O_4$), norfloxacin (NFX, $C_{16}H_{18}FN_3O_3$), rhodamine B (RhB, $C_{28}H_{31}ClN_2O_3$), tert-butanol alcohol (TBA), benzoquinone (BQ), nitrobenzene (NB), benzoic acid (BA), KCl, KNO_3, K_2SO_4, $KHCO_3$, K_2HPO_4, potassium hydrogen peroxymonosulfate (PMS, $2KHSO_5{\cdot}KHSO_4{\cdot}K_2SO_4$), standard solution of hydroxide potassium (KOH, 0.1 mol L^{-1}), nitric acid (HNO_3, 65–68%), and commercial Co_3O_4 nanoparticles with purity of 99% were purchased by Aladdin Company, China. All the chemicals were used as received without further purification. Commercial granular porous alumina (GPA, Sinopharm, Shanghai) with diameter of 1–2 mm was firstly washed using deionized water and then dried overnight at 105 °C prior to further use. Ultrapure water was used throughout our experiments.

2.2. Synthesis of samples

The cobalt−aluminum oxide clusters-embedded γ-Al_2O_3 nanosheets (CAO@AO) were synthesized via a simple "hydrothermal–Co^{2+} adsorption–calcination" process:

Firstly, the precursor of nanosheets-assembled monodispersed hollow γ-AlOOH microspheres was synthesized through a hydrothermal route as follows [28,29]: 1.208 g of $Al(NO_3)_3{\cdot}9\ H_2O$, 0.56 g of K_2SO_4, and 0.40 g of $CO(NH_2)_2$ were dissolved in 64 mL of ultrapure water. The resulting mixed solution was sealed in a Teflon-lined stainless-steel autoclave (100 mL) and heated at 180 °C for 6 h. Afterwards, the autoclave was cooled to room temperature, and the solid product was collected by centrifugation, fully washed with deionized water and anhydrous methanol, and dried to obtain the precursor γ-AlOOH.

Then, five methanolic solutions of $Co(CH_3COO)_2{\cdot}4\ H_2O$ were prepared by dissolving a certain amount of $Co(CH_3COO)_2{\cdot}4\ H_2O$ (0.1, 1.2, 12.5, 124.5, or 622.5 mg) in anhydrous methanol. For each cobalt-containing solution, 300 mg of γ-AlOOH precursor powders were added and fully dispersed. The solvent was then removed by a rotary evaporator, and the solid powders (pale pink) were dried at 60 °C for 12 h. Through these procedures, five Co^{2+}–adsorbed γ-AlOOH with different molar ratios of Co/Al (1:10000, 1:1000, 1:100, 1:10, and 1:5) were obtained.

Finally, the Co^{2+}-adsorbed γ-AlOOH samples were heated in a muffle furnace at 500 °C for 2 h with the heating rate of 5 °C min^{-1} to obtain the target catalysts CAO@AO-x (x = 1, 2, 3, 4, and 5, which correspond to the Co/Al molar ratios 1:10000, 1:1000, 1:100, 1:10, and 1:5, respectively).

Using similar procedures for CAO@AO-2, we synthesized a series of M-substituted (M = Fe, Mn, or Cu) CAO@AO-2 catalysts (denoted as M(y%)-CAO@AO, where y% represents the molar percentage of M/(M+Co)). The total amount of M and Co in M(y%)-CAO@AO was equivalent to the cobalt content in CAO@AO-2. Furthermore, Mn(40%)-CAO@AO-immobilized granular porous alumina (Mn(40%)-CAO@AO/GPA) was also synthesized, and the detailed synthetic procedures are presented in Text S1.

2.3. Sample characterization

The crystal structures of solid samples were analyzed using X-ray diffractometer (XRD, D8-FOCUS, Bruker, Germany). The morphologies of the as-prepared samples were observed by a field-emission scanning electron microscope (SEM, SU8010, Hitachi, Japan) and transmission electron microscope (TEM, TF20, Joel 2100 F) equipped with an energy-dispersive X-ray spectrometer (EDS). Surface chemical states of active sites on samples were surveyed by X-ray photoelectron spectroscopy (XPS) on a PHI5000 Versa Probe (ULVAC-PHI, Japan) with monochromatized Al Kα X-ray radiation (1486.6 eV), where its energy resolution is about 0.2 eV. The binding energy was analyzed in reference to the C 1 s line at 284.8 eV. The infrared spectrum of the dry samples supported on KBr pellets at fixed amount of sample (1 wt%), was recorded on a Nicolet 8700 FT-IR spectrophotometer (Thermo Fisher Scientific Inc., USA). UV–Vis absorption spectra were detected on a spectrophotometer (UV3600, Shimadzu, Japan) with an integrating sphere and $BaSO_4$ was used as the reference sample. The reactive oxygen species (ROSs) were tested by the electron paramagnetic resonance (EPR, Bruker A300). The amount of Co leaching from the tested catalysts was determined by inductively coupled plasma optical emission spectroscopy (ICP–OES, OPTIMA 7000 DV and Optima 5300 DV). The intermediates produced in the MNZ degradation process were determined by liquid chromatograph combined with mass spectrometry (LC–MS, Q Exactive Hybrid Quadrupole-Orbitrap, Thermo Scientific, Bremen, Germany) in ESI positive mode. The Brunauer–Emmett–Teller (BET) surface areas of the samples were analyzed by the N_2 adsorption/desorption on a KASAP2460 system. The total organic carbon (TOC) of MNZ solution was analyzed using a vario TOC analyzer (ELEMENTAR). The test conditions for electron paramagnetic resonance spectroscopy (EPR) and liquid chromatography-mass spectrometry are described in Text S2. Analytical method and operational details regarding the interfacial pH-buffering property of samples are provided in Text S3.

2.4. Evaluation of catalytic performance

The catalytic oxidation degradations of antibiotics metronidazole (MNZ) and other representative pollutants (OFX, NFX, RhB, and MB) were investigated with the use of the as-synthesized powdered samples and PMS as the catalysts and oxidant, respectively. Typically, 0.1 g of CAO@AO-2 powders (Co content of 0.115 mg) were added into an ampoule bottle (20 mL) that contained 10 mL of MNZ solution (10 mg L^{-1}). The ampoule bottle was sonicated for 5 s and then transferred to a constant temperature shaker at 25 °C in dark. Under shaking at a speed of 200 rpm, PMS (1 mM) was added to start the degradation reaction. At a specific interval, 1 mL of the reaction solution was withdrawn and immediately transferred to 1 mL of methanol to terminate the reaction. The solid−liquid separation was achieved with a 0.22 μm syringe, and the solution was measured in a UV−Vis spectrophotometer with the maximum absorption wavelength of 317 nm. The separated solid catalyst powders were fully washed with water/ethanol, dried, and then reused in the next cycle.

To build a column reactor, 10 g of Mn(40%)-CAO@AO/GPA were packed as a fixed bed into a plastic column with an inner diameter of

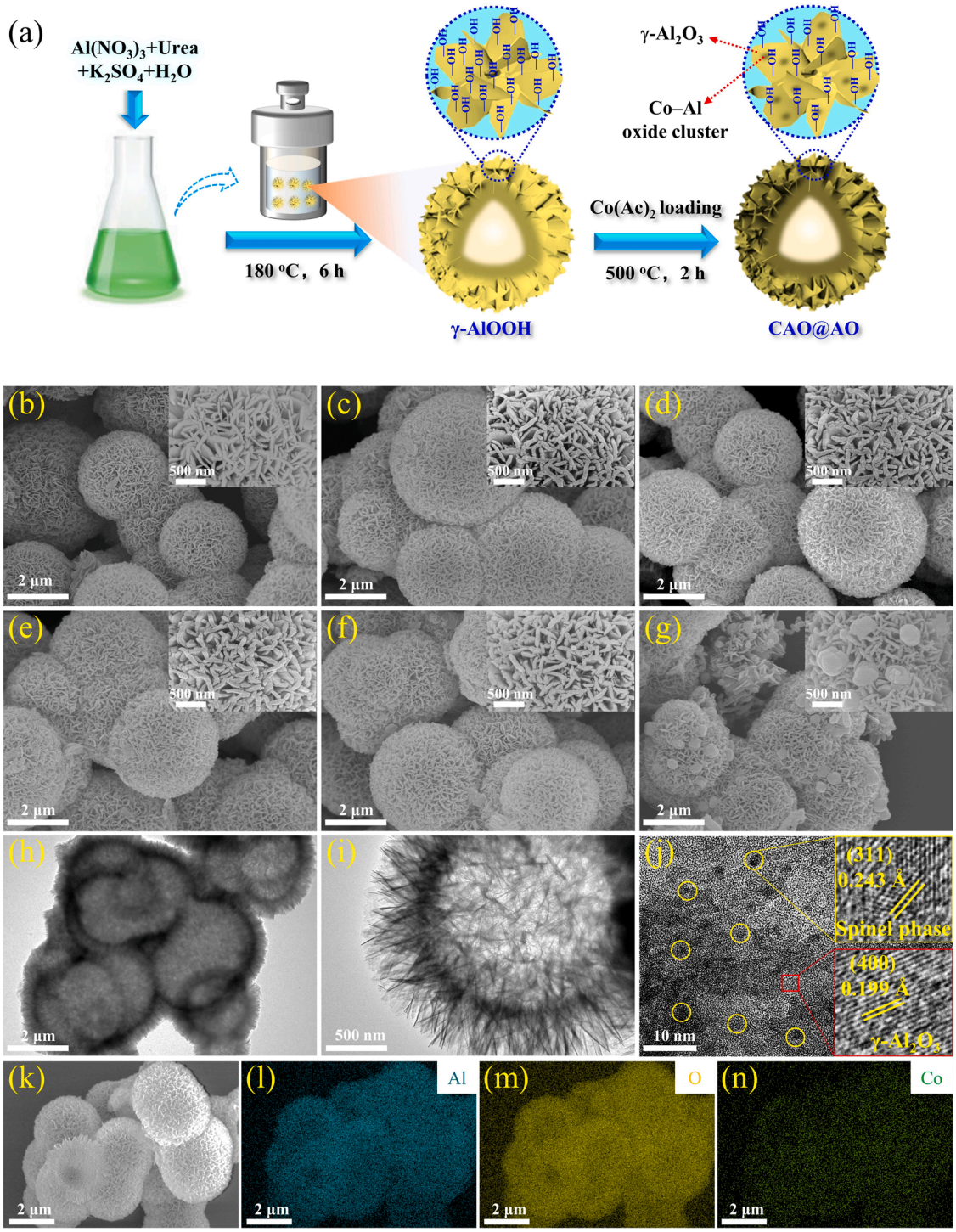

Fig. 1. Material preparation process (a); SEM images of AO (b), CAO@AO-1 (c), CAO@AO-2 (d), CAO@AO-3 (e), CAO@AO-4 (f), and CAO@AO-5 (g); TEM images (h, i) and HRTEM image (j) of CAO@AO-2 and its EDS mapping images (k–n).

10.8 mm and a height of 120 mm. The MNZ solution with a concentration of 10 mg L^{-1} and a volume of 1000 mL was prepared as the organic wastewater. Before the degradation reaction, 1 mM of PMS was added into the MNZ solution, and then the mixed solution was injected into the column reactor by a peristaltic pump at a flow rate of 10 mL min^{-1}. The residual MNZ and cobalt leaching in the solution were monitored by UV–Vis and ICP–OES analyses, respectively.

3. Results and discussion

3.1. Design and physicochemical features of CAO@AO catalysts

In our synthetic protocol, the nanosheets-assembled monodispersed hollow γ-AlOOH microspheres are used as the precursor of catalysts, which can be facilely synthesized via a convenient hydrothermal approach, as demonstrated in literature [28,29]. Considerable research has illustrated that γ-AlOOH with Al−OH-rich surface can effectively capture transition metal cations (e.g., Co^{2+}) through surface complexing [30–33]. Moreover, it is well established that the γ-AlOOH can be readily transformed into γ-Al_2O_3 under mild calcination conditions with almost unchanged morphology [34,35]. Based on these facts, we rationally speculate that the cobalt−aluminum oxide clusters-embedded γ-Al_2O_3 nanosheets (CAO@AO) can be obtained by a "hydrothermal–Co^{2+} adsorption–calcination" process (Fig. 1a), which will exhibit a hierarchical hollow morphology with large surface area and highly open pore structure. More significantly, it is further anticipated that the surface of CAO@AO with abundant hydroxyls groups (≡Al−OH) is capable of buffering the local pH around the particle surface to approximately neutral levels due to the active protonation/deprotonation of ≡Al−OH [36,37]. The ≡Al−OH-induced local pH maintenance at neutrality, if realized, will be of great significance with respect to safeguards that prevent cobalt leaching from the resulting CAO@AO. To verify whether the structure and composition of the target catalysts are developed as expected, the CAO@AO-*x* (*x* represents the Co/Al molar ratio, $x = 1$, 2, 3, 4, and 5) and the control samples were analyzed by multiple techniques, including SEM, HRTEM, XRD, UV−Vis DRS, XPS, and N_2 adsorption−desorption.

SEM characterization was first carried out to obtain the morphological information of the as-synthesized samples, and the results are shown in Fig. 1. From the Fig. 1b, it is evident that the γ-AlOOH precursor is fully composed of monodispersed microspheres with size of about 1.5–2 μm. Each microsphere is constructed by intertwined two-dimensional (2D) ultrathin nanosheets, which exhibits a flowerlike architecture. Such a hierarchical structure with highly accessible surface should be fairly advantageous for the subsequent adsorption of Co^{2+} ions. Upon calcination, the Co^{2+}–loaded γ-AlOOH intermediates with various Co^{2+} contents were transformed into CAO@AO-*x* ($x = 1$–5) samples, and their SEM images are presented in Fig. 1c–g. Interestingly, it can be observed that all the CAO@AO-*x* samples remain the flower-like morphology without any structure destruction, indicating their good structural stability during the thermal treatment. As the cobalt content further increases to Co/Al = 1:5, some nanoparticles of average sizes about 300–500 nm are formed on the surface of nanosheets (CAO@AO-5, Fig. 1g), which are likely to be cobalt oxide. To further reveal the morphological features, the typical sample CAO@AO-2 (Co/Al = 1:1000) was characterized by HRTEM, and the results are displayed in Fig. 1h–j. Clearly, it can be seen that a large inner hollow space with diameter of about 1.5–2.0 μm is surrounded by well-assembled nanosheets (Fig. 1h). These measurements clearly indicate that the as-synthesized sample possesses a desired morphology of hierarchical hollow microspheres. Further observations on the nanosheet of an individual hollow microsphere confirm that its surface is smooth without any extraneous particles (Fig. 1i). The presence of cobalt−aluminum oxide cluster in the CAO@AO-2 is also verified by the higher-magnification TEM image, as shown in Fig. 1j. In more detail, lattice fringes observed from this TEM image indicate that some fine $CoAl_2O_4$ clusters (2–5 nm) are uniformly embedded into the γ-Al_2O_3 nanosheets. To further verify the overall uniformity of $CoAl_2O_4$ clusters in the surface of γ-Al_2O_3 support, the CAO@AO-2 sample was tested by EDS mapping. As shown in the Fig. 1k–n, Co, Al, and O elements are evenly distributed within the whole microsphere [38,39]. Furthermore, the consents of Co and Al in CAO@AO-*x* ($x = 1$–5) were determined by ICP−OES, and the results are summarized in Table S1. Based on these data, the molar ratios of Co/Al in CAO@AO-1, CAO@AO-2, CAO@AO-3, CAO@AO-4, and CAO@AO-5 are estimated to be 1:9345, 1:1063, 1:114, 1:9.6, 1:5, respectively, which are basically consistent with the expectations. Overall, these results confirm the effectiveness of our synthetic protocol.

To determine phase structures of the as-synthesized samples, the XRD characterization was conducted. As shown in Fig. 2a, the control sample AO, obtained from direct calcination of γ-AlOOH in the absence of cobalt salt, presents three characteristic peaks at 37.6°, 45.8°, and 67.0°, which correspond to the (311), (400), and (511) crystal planes of γ-Al_2O_3 (JCPDS PDF 04–0858), respectively. This is consistent with the reported results [40,41], confirming the effective transformation of γ-AlOOH into γ-Al_2O_3 under calcination conditions. Subsequently, the XRD measurements on the samples obtained from the calcination of Co^{2+}-adsorbed γ-AlOOH intermediates were also performed. It can be seen that the XRD patterns of both CAO@AO-1 and CAO@AO-2 are rather similar to that of AO. The absence of diffraction signal for cobalt-containing oxide should be explained by the extremely low contents of cobalt in the two samples (Co/Al ≤ 1:1000). As the cobalt content increases to Co/Al = 1:100 and 1:10, the resulting CAO@AO-3 and CAO@AO-4 exhibits characteristic peaks of γ-Al_2O_3 and spinel phase, where the diffraction intensities of the spinel phases are relatively weak due to their low contents. In theory, the spinel phase possibly corresponds to three crystalline phases: cobalt–cobalt Co_3O_4 (JCPDS PDF 44–0160), cobalt–aluminum $CoAl_2O_4$ (JCPDS PDF 09–0418), or aluminum–aluminum Co_2AlO_4 (JCPDS PDF 38–0814). The three crystalline phases cannot be effectively distinguished by XRD technique because their characteristic peaks are very close in both position and intensity [42]. When the cobalt content reaches Co/Al = 1:5, the CAO@AO-5 sample only shows the characteristic peaks of spinel phase, implying a sufficient transformation of alumina in the presence of high-content cobalt species.

Above-mentioned characterizations fail to adequately confirm the types of Co-based species in the CAO@AO catalysts. Therefore, the UV–Vis DRS technique was employed on account of its ability to probe metal species and their coordination chemistry in various solid substrates. As shown in Fig. 2b, when the cobalt contents are low (CAO@AO-*x*, $x = 1$, 2, and 3), the samples are blue in color and three absorption peaks appear at 543, 580, and 627 nm, which can be attributed to the $^4A_2(F) \rightarrow {}^4T_1(P)$ transition of tetrahedral Co^{2+} coordination, indicating that $CoAl_2O_4$ is the main spinel phase in the three samples [39,43–45]. The $CoAl_2O_4$ should be formed through the migration of Co^{2+} ions to the tetrahedral sites of the γ-Al_2O_3 lattice. When the cobalt content reaches Co/Al = 1:10 (CAO@AO-4), the sample becomes green and two absorption bands are observed at 408 and 644 nm. The absorption peak at 408 nm is attributed to the ligand–to–metal charge transfer (LMCT) process of $O^{2-} \rightarrow Co^{2+}$ (tetrahedral T_d), whereas the absorption peak at 644 nm should result from the ligand–to–metal charge transfer (MLCT) process of $O^{2-} \rightarrow Co^{3+}$ (octahedral O_h), which are indicative of Co_2AlO_4 phase [38]. When the cobalt content is further increased (CAO@AO-5), the sample is black and two wide bands at 368 and 702 nm appear, which should originate from the Co_3O_4 phase [46].

The chemical composition and valence states of cobalt elements in the as-synthesized samples were investigated by XPS technique, and the results regarding the typical sample CAO@AO-2 are shown in Fig. 2c and d. The wide-scan XPS spectrum reveals the presence of Co, Al, and O elements (Fig. S1), where the C 1 s signal should be due to the exposure of the sample to a substrate environment containing carbon-based

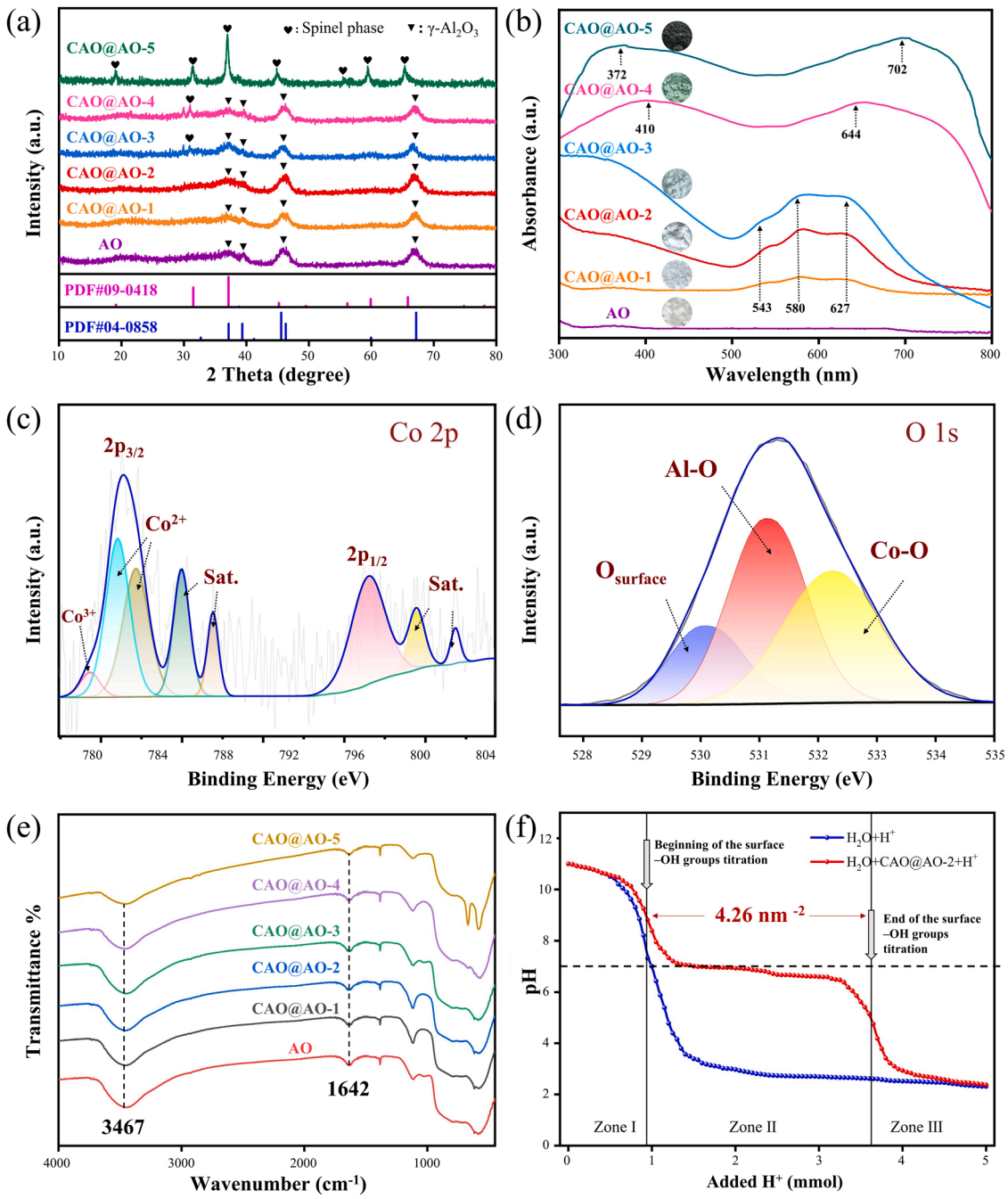

Fig. 2. XRD patterns (a) and UV–Vis DRS spectra (b) of AO and CAO@AO catalysts; high resolution XPS spectra of Co 2p (c) and O 1 s (d) in CAO@AO-2; FT-IR spectra of AO and CAO@AO catalysts (e); hydroxy titration of CAO@AO-2 (f).

compounds. In the high-resolution XPS spectra of Co 2p, the binding energy at 779.9 eV can be assigned to Co^{3+}, while the binding energies at 780.9 and 782.3 eV correspond to Co^{2+} species. The other higher binding energies at 786.7 ± 0.1 and 787.5 ± 0.1 eV should be ascribed to the dithered satellite (abbreviated as "Sat") of Co^{3+} and Co^{2+}, respectively [47,48]. This result further indicates that the spinel phase of CAO@AO-2 is mainly $CoAl_2O_4$, which is well consistent with the UV–Vis DRS results. Furthermore, the O 1 s spectrum of the CAO@AO-2 sample can be divided into three sub-peaks (Fig. 2d). The sub-peak at 531.6 eV should be indexed to the surface hydroxyl groups (≡Al–OH), while the sub-peaks at 530.8 and 529.5 eV correspond to lattice oxygens from Al–O and Co–O units, respectively. From the fitting results, it can be inferred that CAO@AO-2 contains a large number of surface hydroxyl groups [49,50].

The presence of surface hydroxyl groups on the CAO@AO-x (x = 1–5) is further confirmed by the FT-IR spectra (Fig. 2e), where the characteristic peaks (corresponding to hydroxyl groups) at 1642 and 3467 cm^{-1} appear for all the samples. Further observation reveals that the characteristic peak intensities of CAO@AO-1, CAO@AO-2, and CAO@AO-3 are similar to that of AO, indicating that the introduction of low content cobalt (Co/Al ≤ 100) in embedded form cannot induce an obvious decrease of hydroxyl groups. Using CAO@AO-2 as the representative sample, we performed an acid titration of its suspension to estimate the content of surface hydroxyl group (The measurement detail is presented in Text S4 and the data are shown in Fig. 2f) [51,52]. Comparing the pure water, the CAO@AO-2 suspension shows a slow drop with the addition of H^+. This is because the surface hydroxyl groups can consume protons according to the reaction: ≡Al–OH + H^+ →

≡Al–OH_2^+. From the two inflection points on the titration curve [27,28], the density of surface hydroxyl groups of CAO@AO-2 is estimated to be 4.26 nm^{-2}, which is in accordance with the reported values for γ-Al_2O_3 [53]. The rich ≡Al–OH groups on the surface of CAO@AO-2 are expected to act as heterogeneous buffer species that can control the interfacial pH at nearly neutral levels during subsequent catalysis.

To get insight into the textural parameters (i.e., specific surface area and porosity) of CAO@AO-2, N_2 adsorption−desorption tests were performed. The isothermal curves are shown in Fig. S2a, which can be classified as type III isotherms with a H3 hysteresis loop. To be specific, the hysteresis loop at relative pressure (P/P_0) of 0.7–0.9 should be ascribed to the inner space of the interwoven nanosheets, whereas the hysteresis loop in the higher pressure stage (P/P_0 = 0.9–1.0) should be due to the large void space in the hollow microspheres. According to the Brunauer–Emmett–Teller (BET) method, the specific surface area of CAO@AO-2 is estimated to be about 194.7 $m^2\,g^{-1}$, which is significantly larger than various previously reported heterogeneous cobalt-based catalysts [15,49]. As well known, a solid catalyst with a large specific surface area will provide abundant active sites, which is really beneficial for high-efficiency catalysis. Furthermore, the pore distribution of CAO@AO-2 was estimated by the Barrett–Joyner–Halenda (BJH) equation, and the results are shown in the inset of Fig. S2b. It can be found that the pore sizes of CAO@AO-2 are distributed from several nanometers to more than 60 nm with maxima at 23.7 nm, suggesting that there are plentiful mesopores and macropores in the flower-like structure. A quantitative calculation shows that the total pore volume of CAO@AO-2 reaches 0.62 $cm^3\,g^{-1}$, which is roughly comparable to the reported values for many hierarchical hollow metal oxide analogues [15,54].

3.2. pH-buffering properties of CAO@AO

To investigate the pH-buffering behaviors of CAO@AO, the initial and final pH values of water in the presence of CAO@AO-2 were monitored, and the results are shown in Fig. 3a. In this figure, the final pH is plotted versus the initial pH to give a curve which represents the buffering effect of CAO@AO-2 in water. Clearly, the final pH exhibits a broad plateau in the initial pH range of 4–10, indicating that CAO@AO-2 indeed acts as an effective pH buffering agent. According to the previous studies [55], the pH-buffering properties of CAO@AO-2 should originate from its amphiphilic surface. Specifically, the ≡Al–OH groups on the surface of CAO@AO-2 will undergo both protonation at low pH (< pH_{PZC}) and deprotonation at high pH (> pH_{PZC}), which can be described as follows:

$$\equiv Al\text{–}OH + H_i^+ \rightarrow \equiv Al\text{–}OH_2^+ \quad (1)$$

$$\equiv Al\text{–}OH + OH_i^- \rightarrow \equiv Al\text{–}O^- + H_2O \quad (2)$$

where H_i^+ and OH_i^- represent the proton and hydroxide ion at the interface between CAO@AO-2 and water, respectively. When extra protons or hydroxide ions are presented in the CAO@AO-2/H_2O suspension, they will be readily consumed by the ≡Al–OH groups to maintain the pH at near neutral levels. It is worth mentioning that that adding other oxides (acidic and basic oxides) into water should not be able to buffer the pH around neutrality owing to the following facts: 1) the surface hydroxyl groups of acidic oxides (e.g., SiO_2) is obviously more acidic than ≡Al–OH groups and they are less effective in eliminating protons in the solution; 2) the surface hydroxyl groups of basic oxides (e.g., MgO), as opposed to those of acidic oxides, have a strong

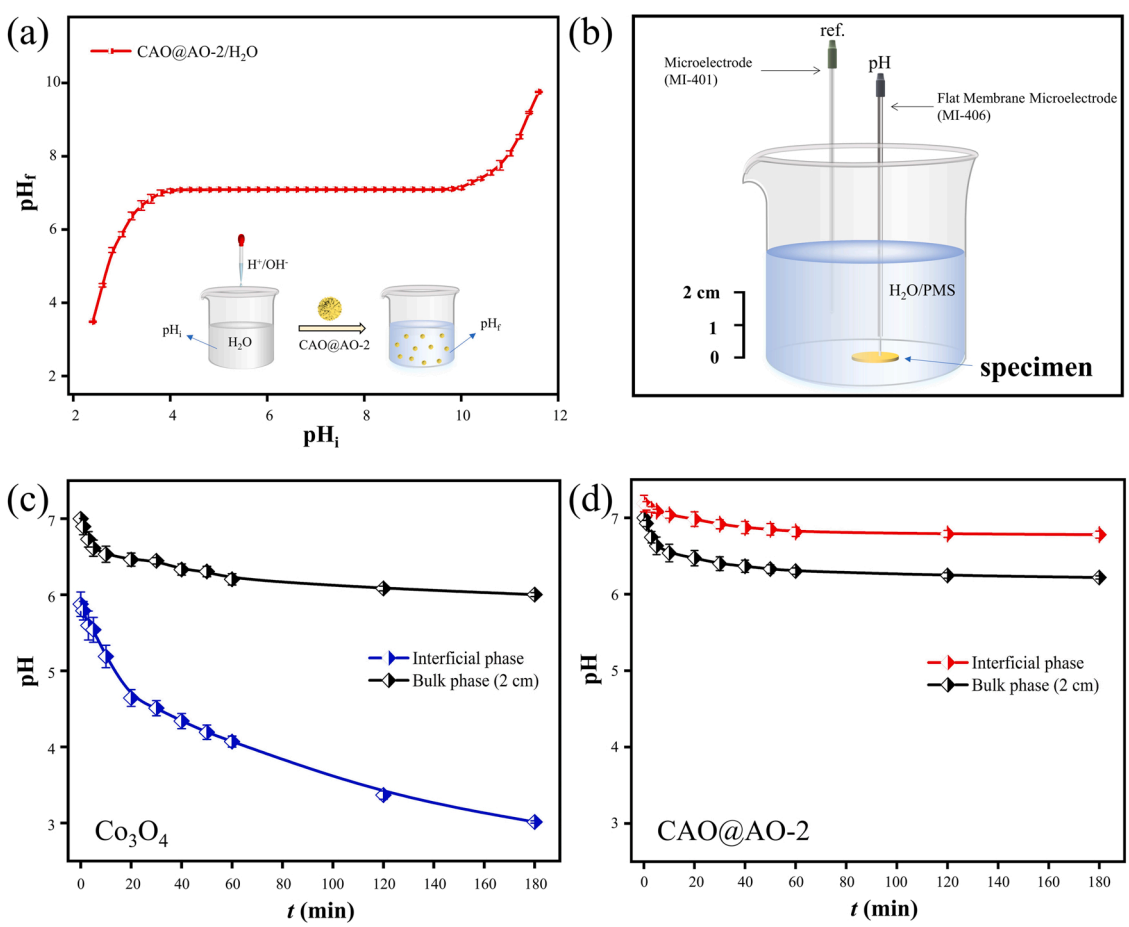

Fig. 3. pH-buffering behaviors of CAO@AO-2 (a); schematic diagram of interface pH measurement (b); pH values at interfacial phase and bulk phase for Co_3O_4 (c) and CAO@AO-2 (d) in the presence of PMS.

tendency to form protonated species, which always make the solution alkaline. Attractively, the CAO@AO-2 contains abundant ≡Al–OH groups and possesses a suitable amphiphilic property, which is expected to show a strong buffering ability for overcoming the cobalt leaching in the activation of PMS.

However, it should be also noted that the above-mentioned pH determinations on CAO@AO-2/H_2O system were conducted simply by monitoring the pH of the bulk phase rather than the interface phase. In fact, the protonation and deprotonation behaviors of ≡Al–OH groups are directly dependent on the proton (H_i^+) and hydroxide ions (OH_i^-) at the interface, as shown in Eqs. 1 and 2. On the other hand, the PMS decomposition is actually induced by the surface sites of solid catalyst, which means that the H^+ is also formed at the solid−liquid interface and then gradually diffused into the bulk phase. Accordingly, the interfacial pH in particular is to be considered, although this has generally been overlooked in the heterogeneous activation of PMS. Considering these facts, we conducted the comparative experiments on monitoring the pH difference between the bulk and interface phases of CAO@AO-2/H_2O/PMS and Co_3O_4/H_2O/PMS, where the CAO@AO-2 and Co_3O_4 powders were pressed into pieces in a 10 mm diameter (Fig. 3b) [56]. During the process of PMS activation, it can be observed that the pH values of both bulk and interface phases of Co_3O_4/H_2O/PMS rapidly decrease (Fig. 3c). Moreover, the interfacial pH values are significantly lower than those of bulk phase in the whole course. This is probably because the release of H^+ mainly occurs in the interfacial regions and its diffusion leads to the concentration gradient. In contrast, the pH values of both bulk and interface phases of CAO@AO-2/H_2O/PMS remains relatively stable levels during PMS activation (Fig. 3d), and the interfacial pH values (6.8–7) are found to be appreciably higher than those (6.1–6.5) of the bulk medium. These phenomena should be due to the strong interfacial pH-buffering ability of CAO@AO-2, which essentially creates an ideal local microenvironment that is beneficial for the cobalt leaching-free activation of PMS.

3.3. Catalytic performance of CAO@AO in activating PMS for MNZ degradation

Catalytic behaviors of the as-obtained CAO@AO catalysts were systematically evaluated by activating PMS for MNZ removal. Fig. 4a displays the removal efficiencies of MNZ in different reaction systems. Sole addition of CAO@AO catalyst (e.g., CAO@AO-2) or PMS into the MNZ solution only gives rise to a low removal efficiency (< 4%). The results clearly indicate that the adsorption of MNZ on the CAO@AO is basically negligible, and unactivated PMS has a rather weak oxidation ability toward MNZ. In contrast, the MNZ can be effectively degraded in the CAO@AO/PMS systems. Although the removal efficiency of MNZ is relatively low (~58% within 20 min) in CAO@AO-1/PMS system due to the extremely low cobalt content in CAO@AO-1 (Co/Al = 1:10000), all the MNZ molecules can be rapidly eliminated within 5 min in other systems (catalysts: CAO@AO-2, CAO@AO-3, CAO@AO-4, and CAO@AO-5), suggesting that the CAO@AO catalysts have remarkable catalytic activities for PMS activation. The slight deference of catalytic efficiency between the four catalysts should be due to the varied contents of cobalt. Table S2 lists the removal performance of MNZ by CAO@AO-2 and several previously reported solid cobalt-based catalysts. It can be seen that the CAO@AO-2 possesses obviously higher activity as

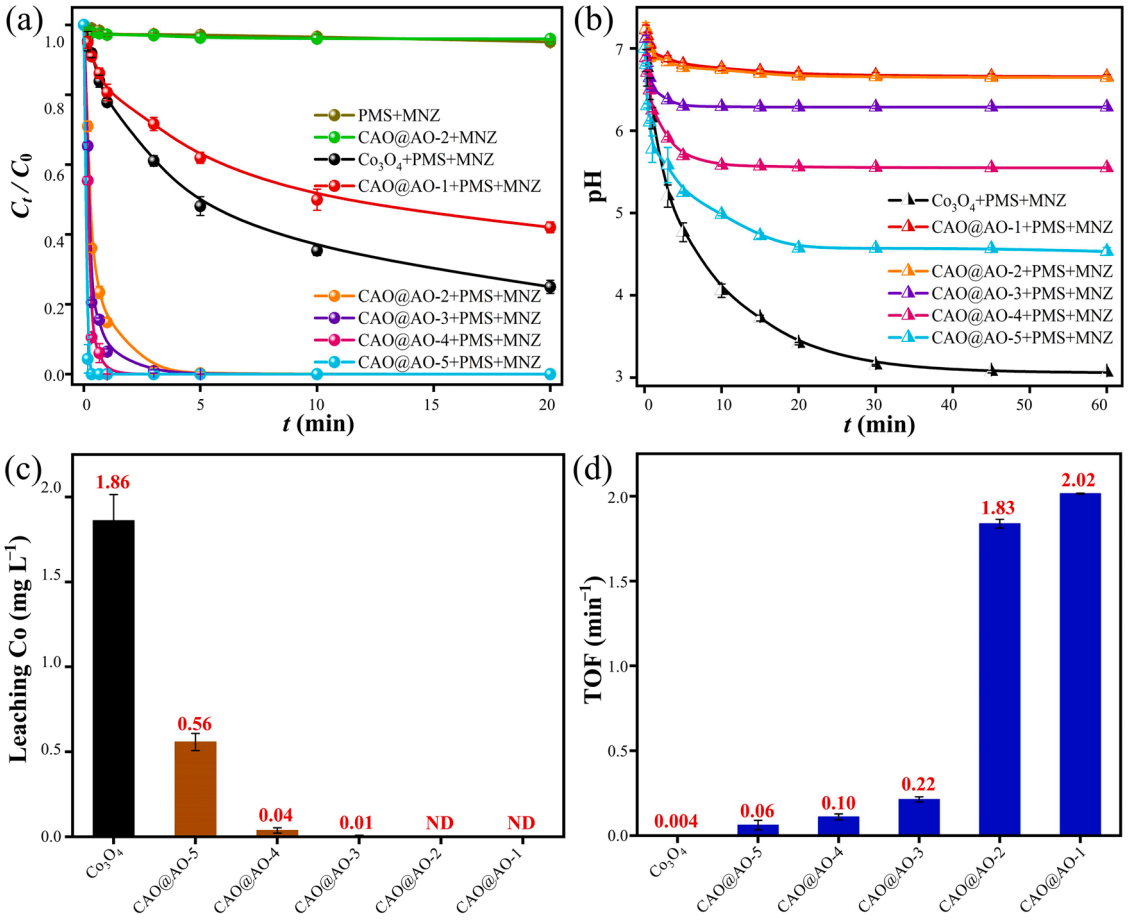

Fig. 4. Catalytic degradation curves (a); pH vlues during MNZ degradation in different systems (b); leached Co amount (c) and TOF values (d) of Co_3O_4 and CAO@AO catalysts. (Experimental conditions: $V = 10$ mL; $C_{MNZ} = 10$ mg L^{-1}; $C_{PMS} = 1$ mM; pH = 7; $t = 25$ °C; [CAO@AO] = 10 g L^{-1} (due to very low content of cobalt), [Co_3O_4] = 1 g L^{-1}).

compared to the others. Moreover, under the identical reaction conditions, the control catalyst (Co_3O_4) shows a rather limited catalytic ability for MNZ removal (Fig. 4a), which further highlights the superior catalytic performance of CAO@AO.

During MNZ degradation, the pH values of above-mentioned catalytic oxidation systems were also monitored, and the results are shown in Fig. 4b. With use of Co_3O_4 as catalyst, the solution pH decreases quickly with time, which should be ascribed to the continuous release of H^+ along with the activation of PMS. As a consequence, the cobalt leaching from Co_3O_4 reaches up to 1.86 mg L^{-1}, which is, more or less, consistent with those previously reported results from various unbuffered cobalt-based solid catalysts [57–60]. Fig. 4b also shows that the pH drops of CAO@AO/PMS/MZN systems are much lower than that of Co_3O_4/PMS/MZN, which should be due to the pH-buffering properties of CAO@AO. The reduced change in pH is indeed effective for minimizing the cobalt leaching (Fig. 4c). In particular, the pH values of CAO@AO-1/PMS/MNZ and CAO@AO-2/PMS/MNZ systems are found to be nearly neutral and very stable during the period of 60 min. Under such circumstances, the cobalt leaching is completely avoided (Fig. 4c).

To better understand the catalytic behaviors of CAO@AO catalysts, their turnover frequencies (TOF) were calculated (the calculation detail is presented in Text S5). As shown in Fig. 4d, the TOF values of CAO@AO catalysts are in the range of 0.06–2.02 min^{-1}, which are obviously higher than that (0.004 min^{-1}) of Co_3O_4. Impressively, the CAO@AO-2 not only enables complete and rapid degradation of MNZ (Fig. 4a), but also exhibits a high TOF (1.83 min^{-1}), which is about 475.5 times higher than that of Co_3O_4 (Fig. 4d). Besides, it is also observed that the TOF values of CAO@AO catalysts gradually enhance with the decrease of cobalt content (Fig. 4d). One possibility might be that the CAO@AO catalysts with lowed cobalt contents will possess a relatively higher amount of surface ≡Al–OH groups to better promote the cobalt-mediated PMS activation, as discussed later (Section 3.4).

In light of the fact that a number of factors (e.g., initial solution pH, PMS dosage, MNZ concentration, catalyst dosage, coexisted anions, and reaction temperature) might influence the catalytic performance of CAO@AO, the CAO@AO-2/PMS-induced MNZ degradation under different conditional parameters were also investigated. As shown in Fig. S3, the CAO@AO-2 catalyst exhibits high and almost unchanged catalytic performance at pH values of 3.3–9, which should be due to its strong pH-buffering property that is capable of stabilizing the solution pH at nearly natural levels. Under strong acid conditions (e.g., pH = 1), the CAO@AO-2 is not strong enough to deplete the excess protons; moreover, there is a strong stabilization effect of H^+ ion on the HSO_5^- anions [61,62]. Consequently, the degradation of MNZ at pH 1 is somewhat inhibited (Fig. S3). At pH 11, the slight decrease of MNZ removal efficiency should due to the partial decomposition of PMS by reaction with OH^- (Fig. S3) [3,21,22]. Furthermore, based on the investigations regarding the PMS dosage and MNZ concentration, it is revealed that a low dosage of PMS (≥ 1 mM) can effectively eliminate the MNZ with concentration of 5–15 mg L^{-1} in a short period of time (< 10 min) (Fig. S4). Fig. S5a shows the effect of catalyst dosage on MNZ removal efficiency. It can be found that in the dosage range of 2–10 g L^{-1} the degradation efficiency of MNZ increases significantly with the increase of catalyst dosage. Further increase of catalyst dosage to 20 g L^{-1} does not result in significant enhancement of degradation efficiency. Thus, the catalyst dosage of 10 g L^{-1} is suitable in our catalytic oxidation systems. Besides, we monitored the final pH (pH_f) values and cobalt leaching amount under different catalyst dosage. As shown in Fig. S5b, when the catalyst concentration is low (< 10 g L^{-1}), the number of ≡Al−OH groups might be not enough to fully consume the released H^+, resulting in relatively low pH_f values and slight leaching of cobalt. Fig. S6 shows the effects of several common inorganic anions (NO_3^-, SO_4^{2-}, Cl^-, HPO_4^{2-}, and HCO_3^-, 10 mM) on the MNZ removal efficiency. It can be seen that the addition of NO_3^- and SO_4^{2-} anions have a negligible effect on MNZ degradation, while the introduction of Cl^-, HPO_4^{2-}, or HCO_3^- results in the inhibition of MNZ degradation. This inhibition phenomenon is in line with previous studies, which is due to the consumption of SO_4^-• by these anions with generation of less active radicals (e.g., Cl•, HCO_3•, and HPO_4^-•) [63–65]. Fig. S7 reveals that the rise of temperature can accelerate the degradation of MNZ, which should be ascribed to the endothermic character of PMS activation [38, 66]. The reaction rate constants (k) are estimated to be 0.0667, 0.4466, and 1.0969 min^{-1} at 20, 25, and 30 °C, respectively. The Arrhenius activation energy (E_a = 76.2 kJ mol^{-1}) of degradation reaction falls into a low range of 60–80 kJ mol^{-1}, suggesting that only a low energy barrier needs to overcome for the MNZ degradation in CAO@AO-2/PMS system.

3.4. Plausible degradation pathway and catalytic mechanism

To identify the intermediate products and further ascertain the degradation pathway of MNZ in our catalytic oxidation system, the LC–MS/MS analyses on the reaction solution of CAO@AO-2/PMS/MNZ were performed. As shown in Fig. 5a, the characteristic peak of MNZ (m/z = 171.813) disappears within 10 min, while several new MS signals are observed, indicating the formation of some intermediates during the degradation process. The chemical formulas and mass/charge (m/z) ratios of the intermediate products are figured out and summarized in Table S3. Overall, the degradation of MNZ by CAO@AO-2/PMS includes hydroxylation, ring-opening, denitrification, oxidation, and bond cleavage reactions (Fig. S8), which can be roughly divided into two pathways. In the first pathway, MNZ undergoes hydroxylation to yield an intermediate product P1 (m/z = 189.437), and then the P1 is further oxidized to form carboxylation product (P2, m/z = 201.531). P2 is further transformed to P3 (m/z = 161.213) and P5 (m/z = 141.811) by a combined process involving decarboxylation, dehydrogenation, nitro hydroxylation, and so on. In the second pathway, MNZ should undergo nitro hydroxylation to form the intermediate P4 (m/z = 141.811), which is further converted to P5 via hydroxylation and dehydrogenation. Subsequent oxidative ring opening of P5 results in the formation of P3. Then, the intermediate P3 will be decomposed into the smaller molecules P6 (m/z = 148.521), P7 (m/z = 121.427), and P8 (m/z = 104.374). With prolonged reaction time, these intermediate compounds will be gradually mineralized to CO_2, H_2O, and NO_3^-. At the end of the degradation reaction, the mineralization degree of MNZ was measured by the total organic carbon analyzer. It is found that the 83% of TOC are removed within 10 min, indicating that most MNZ molecules are mineralized, which is superior to the previously reported results (Table S2).

To unveil the types of reactive oxygen species (ROSs) in the CAO@AO-2/PMS/MZN system and their contributions to the MNZ degradation, the EPR characterization and quenching tests were conducted. From Fig. 5b, it can be seen that sole presence of PMS in the MNZ solution will not induce any obvious signal in the detection range (324–334 mT), which suggests that PMS is rather stable and cannot effectively generate free radicals via self-decomposition. In contrast, upon addition of CAO@AO-2 catalyst into the PMS/MNZ solution (containing DMPO as the free radical spin trapping agent), multiple distinct signal peaks appear in the EPR spectrum (Fig. 5b). According to the literature [23], these signals can be rationally assigned to DMPO–OH and DMPO–SO_4 complexes, respectively, indicating the coexistence of SO_4^-• and •OH radicals in the CAO@AO-2/PMS/MNZ system. To further gain insight into the contributions of SO_4^-• and •OH radicals in the degradation of organic matter, we also performed quenching experiments separately using MeOH and TBA as radical scavengers. In fact, it is well documented that MeOH with α-H can effectively scavenge both SO_4^-• and •OH radicals ($k_{SO_4^-\bullet}$ = 1.6–7.8 × 10^7 M^{-1} s^{-1}, $k_{\bullet OH}$ = 1.2–1.8 × 10^9 M^{-1} s^{-1}), whereas TBA is far more effective in capturing •OH than SO_4^-• ($K_{\bullet OH}$ = 3.8–7.6 × 10^8 M^{-1} s^{-1}, Kso_4^- = 4.0–9.1 × 10^5 M^{-1} s^{-1}) [24,67,68]. As shown in Fig. 5c, the addition of TBA into the CAO@AO-2/PMS/MNZ system induces a slight decrease in removal

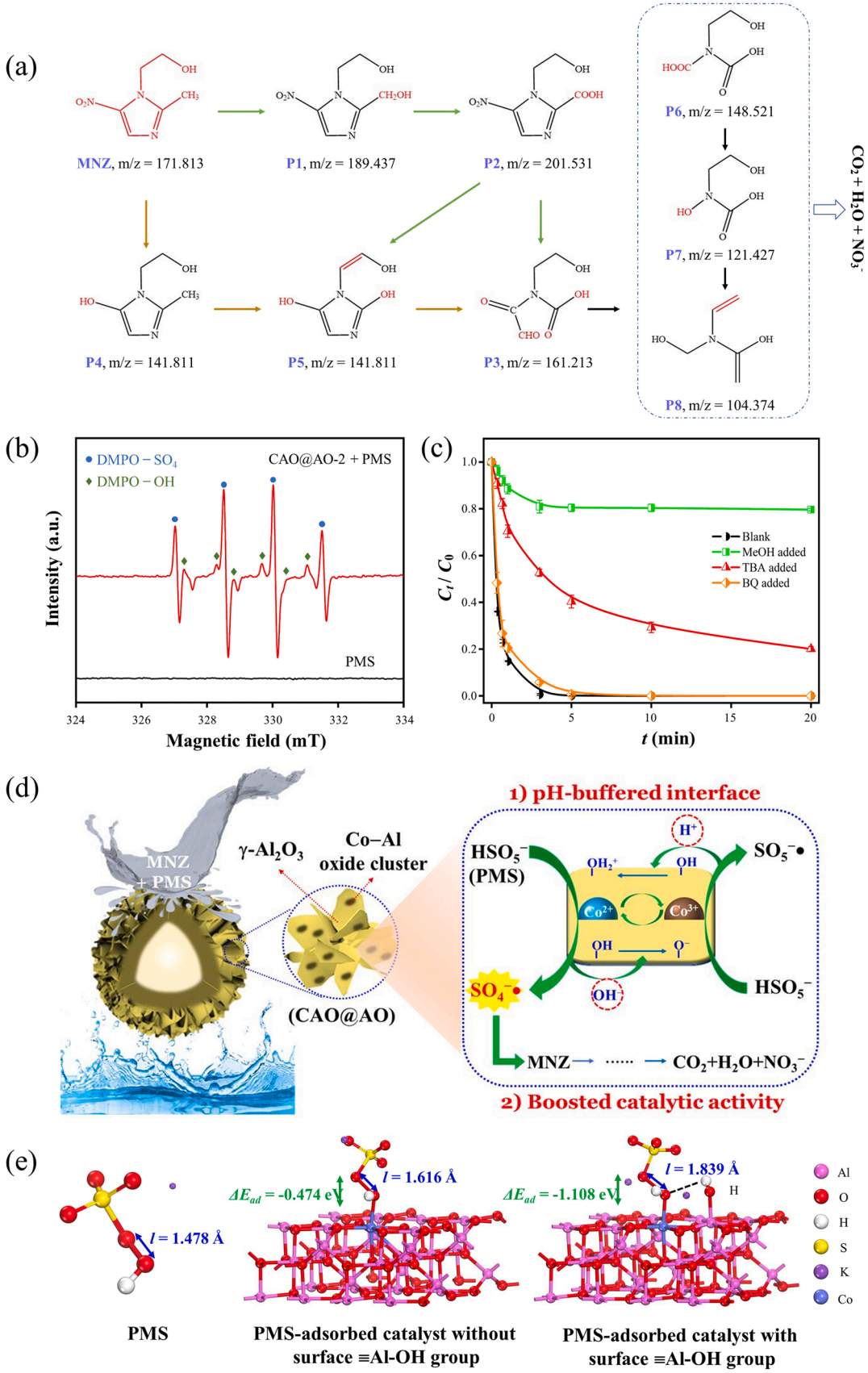

Fig. 5. Degradation pathways of MNZ (a); EPR spectra for two systems (b); quenching results (c); plausible mechanism of catalytic degradation (d); and DFT configurations on PMS before and after adsorption onto Co-containing γ-Al_2O_3 with and without surface ≡Al–OH group (e).

efficiency of MNZ. However, the MNZ degradation is almost completely stopped upon introduction of MeOH. Such significantly different quenching behaviors between TBA and MeOH strongly indicate that $SO_4^{\bullet-}$ is the dominant radical during MNZ degradation. The small portion of •OH radical might be generated according to the following process: $SO_4^{\bullet-} + H_2O \rightarrow SO_4^{2-} + \bullet OH + H^+$ [23]. To confirm whether $^1O_2$ was formed in the catalytic oxidation system, the quenching experiment with benzoquinone (BQ) as scavenger was also conducted. It is found that the presence of BQ cannot induce significant decrease of MNZ degradation (Fig. 5c), indicating that the singlet oxygen is basically negligible in the catalytic oxidation system. Moreover, the aforementioned cyclic voltammetry (CV) and XPS analyses have revealed that the active cobalt species of catalyst are basically consisted of Co^{2+} and Co^{3+} without co-presence of high-valent species (e.g., Co^{4+}), implying that the PMS activation was primarily driven by the Co^{2+}/Co^{3+} redox cycle rather than Co^{4+} [69].

Furthermore, in order to distinguish the contribution of •OH, $SO_4^{\bullet-}$, and possible nonradical species to the MNZ degradation, competitive kinetic experiments were carried out by using a mixed system containing nitrobenzene (NB), benzoic acid (BA), and metronidazole (MNZ). NB can be regarded as a specific probe of •OH and has negligible reactivity with $SO_4^{\bullet-}$ [70]. In contrast, BA can effectively react with both •OH and $SO_4^{\bullet-}$ [70]. The removal rates of NB, BA, and MNZ in the mixed system with time are shown in Fig. S9a. It can be found that MNZ and BA are significantly removed, while the removal efficiency of NB is low, indicating that the major ROS in this system is $SO_4^{\bullet-}$, which is consistent with the results from EPR analyses and above-mentioned quenching experiments. Furthermore, based on the reported methods [70,71], the contributions of •OH, $SO_4^{\bullet-}$ and nonradical oxidation are 13.1%, 82.3%, and 4.6%, respectively (The calculation detail is presented in Text S6 and the data are shown in Fig. S9b, c). The results further indicate $SO_4^{\bullet-}$ is the major ROS for pollutant degradation and the nonradical species only have a very low content in the catalytic oxidation system.

Based on the discussion above, the catalytic mechanism of CAO@AO-2 in activating PMS for MNZ degradation is proposed (Fig. 5d). The highly exposed Co species of CAO@AO-2 serve as the active sites, which are responsible for PMS activation to generate free radicals. The activation process can be briefly expressed as follows [17]:

$$Co^{2+} + HSO_5^- \rightarrow Co^{3+} + SO_4^{\bullet-} + OH^- \quad (3)$$

$$Co^{3+} + HSO_5^- \rightarrow Co^{2+} + SO_5^{\bullet-} + H^+ \quad (4)$$

Unlike other cobalt-based solid catalysts, the CAO@AO-2 possesses abundant and amphiphilic ≡Al–OH groups, which can boost the catalytic ability of cobalt sites. In more detail, the released OH^- ions (Eq. 3) can be effectively assumed by the ≡Al–OH groups to facilitate the transformation of PMS (HSO_5^-) to $SO_4^{\bullet-}$ radical. Meanwhile, the regeneration of Co^{2+} can be also accelerated by the reaction of the released H^+ (Eq. 4) with ≡Al–OH groups. Under the attack of highly powerful radicals, the MNZ molecules can be decomposed into a series of intermediates (P1–P8) and ultimately mineralized into those environmentally bengin products (e.g., CO_2, H_2O, and NO_3^-).

It should be emphasized that the $SO_4^{\bullet-}$ radical is a consequence of the catalytic decomposition of PMS by the surface sites of CAO@AO-2, which has a very short life span (30–40 μs) and its migration distance is also very limited (about 0.5 μm) [72,73]. Moreover, during reaction with MNZ and those intermediates, $SO_4^{\bullet-}$ will ultimately evolve into SO_4^{2-}, which will cause synchronous generation of H^+ to maintain charge balance. Therefore, it is inferable that H^+ will be formed in the interface phase. Fortunately, benefiting from strong pH-buffering ability, the CAO@AO-2 catalyst can stabilize the interfacial pH at nearly neutral level and thus shows a cobalt leaching-free behavior in activating PMS for MNZ degradation.

To better understand the role of surface ≡Al–OH group on the CAO@AO-2 catalyst in the PMS activation, the theoretical calculations based on density functional theory (DFT) was conducted. For simplification purpose, the structural models, i.e., Co-containing γ-Al_2O_3 with and without surface ≡Al–OH group, were adopted. The computational details can be found in Text S7, and the front, left, and top views of the optimized catalyst structures are shown in Fig. S10. In light of the fact that the adsorption of oxidant molecules onto the catalyst surface is a prerequisite for the subsequent activation, the adsorption energy (E_a) of a PMS molecule onto the Co site of catalyst was calculated. It is revealed that the presence of ≡Al–OH group on the surface of catalyst can promote the PMS adsorption, as evidenced by the E_a values (i.e., −1.108 eV for Co-containing γ-Al_2O_3 with surface ≡Al–OH group and −0.474 eV for Co-containing γ-Al_2O_3 without surface ≡Al–OH group, respectively) (Fig. 5e). Furthermore, to ascertain the difference between the two catalysts with regard to their activation efficacies toward PMS, the O–O bond length ($l_{O–O}$) of PMS before and after adsorption was calculated. The $l_{O–O}$ in free PMS molecule exhibits a value of 1.478 Å, while the $l_{O–O}$ is remarkably lengthened for the PMS after being adsorbed on the surfaces (Fig. 5e), suggesting the effective PMS activation by both of the two catalysts. Interestingly, the $l_{O–O}$ value (1.839 Å) of the PMS adsorbed on the catalyst with surface ≡Al–OH group is significantly larger than that (1.616 Å) on the catalyst without surface ≡Al–OH group, indicating that the former has a stronger bond-weakening ability. Based on the above theoretical investigations, it can be inferred that the presence of surface ≡Al–OH on the catalyst can strengthen the adsorption and activating abilities of Co sites for PMS, which leads to a boosted catalytic activity.

3.5. Universal applicability, practical feasibility, and reusability of CAO@AO

To elucidate the universal applicability of the CAO@AO-2 catalyst, we utilized it as the catalyst of PMS to degrade two other common antibiotics (OFX and NFX; 10 mg L^{-1}) and two representative organic dyes (RhB and MB; 30 mg L^{-1}), and the results are presented in Fig. S11. It can be intuitively seen that all the tested organic pollutants exhibit high degradation rates within a short period of time (< 10 min). Especially for OFX and NFX, their degradation degrees reach 98% within 1 min. These findings fully verify the broad potential application scope of CAO@AO-2 as a new PMS activator for the efficient degradation of various refractory organic pollutants in wastewater. Further, in order to explore the practical feasibility of CAO@AO-2, a series of degradation experiments were conducted in the actual water matrixes (taken from tap water, local lake, and fountain water). As shown in Fig. S12, the complete degradation of MNZ only takes about 10 min in all cases, suggesting that CAO@AO-2 holds great promise for practical application.

Then, successive catalytic degradation experiments were performed to evaluate the reusability and stability of CAO@AO-2. As shown in Fig. 6a, this catalyst does not exhibit any activity decay after 15 consecutive cycles. It should be mentioned that for the successive catalytic processes, an intermittent alkali treatment on CAO@AO-2 (i.e., washing this catalyst with dilute KOH solution (pH = 10) every 5 times) is adopted, which proves effective in stabilizing the pH at an appropriate level (> 5) and preventing the cobalt leaching from the catalyst (Fig. 6b). Comparing with some recently reported heterogeneous cobalt-based PMS activators, such as Co_3O_4-Bi_2O_3 (~15% activity loss after 5 cycles) [63], Co_3O_4/NGA (12% activity loss after 5 cycles) [74], $CoFe_2O_4$ (32% activity loss after 5 cycles) [12], and Co(OH)F@MXenes (20% activity loss after 4 cycles) [75], the CAO@AO-2 exhibits a significantly better catalytic stability. More importantly, the CAO@AO-2 with strong pH-buffering property is capable of absolutely avoiding cobalt leaching, which can distinguish it from various ever-reported heterogeneous cobalt-based catalysts. The content of surface hydroxyl group on CAO@AO-2 after 15 successive cycles was measured, and the results are shown in Fig. S13). It is found that the content of surface hydroxyl group on CAO@AO-2 is 4.08 nm^{-1}, which is close to its original value, indicating good stability of surface hydroxyl

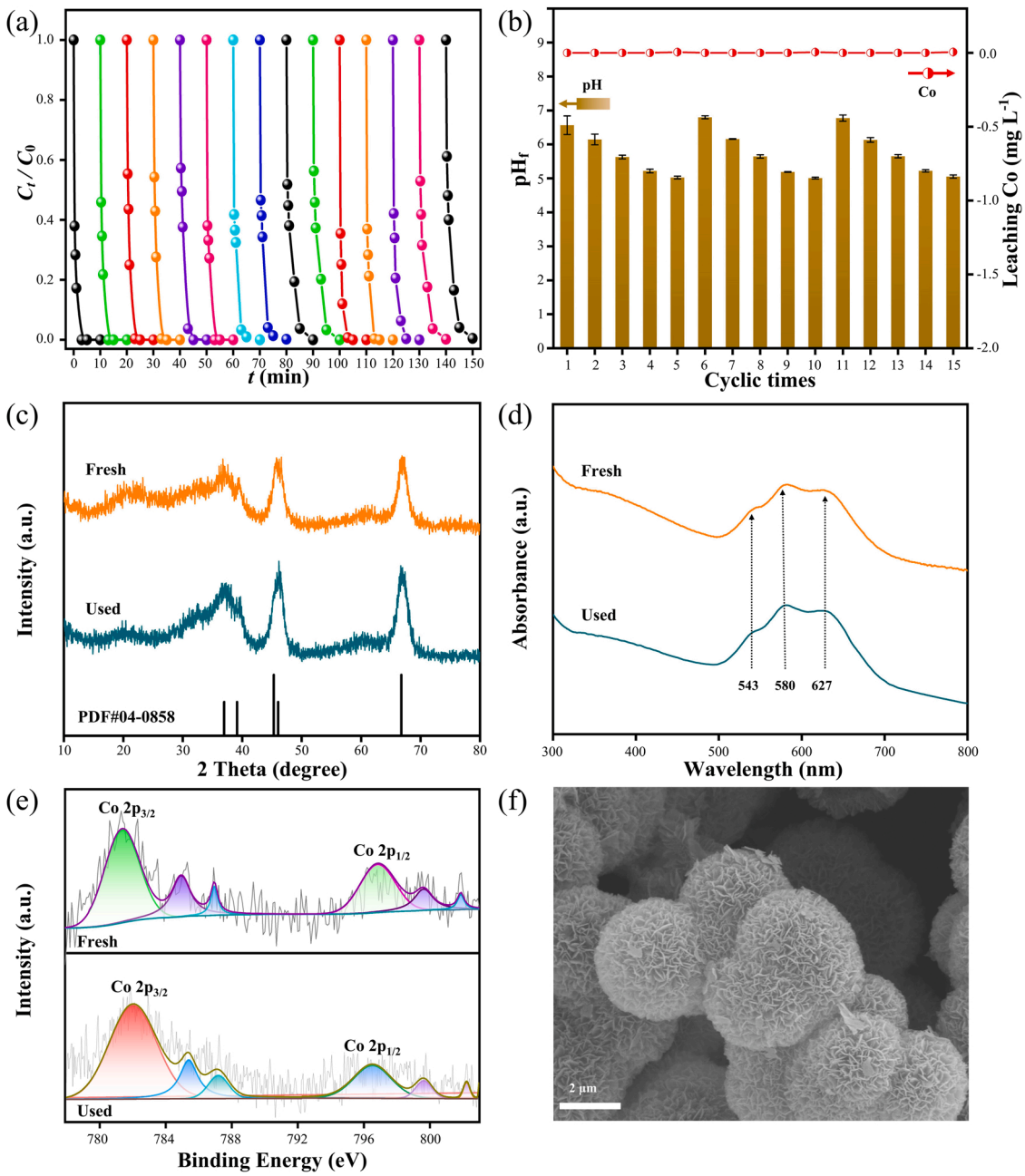

Fig. 6. Catalytic degradation curves during successive use (a); final pH and Co leaching values during successive use (b); XRD patterns (c), UV−Vis DRS spectra (d), XPS spectra (e), and SEM image (f) of catalyst before and after use.

group during cycling use. In addition, we analyzed the exhausted catalyst by XRD, UV−Vis DRS, XPS, and SEM techniques, and the results are shown in Figs. 6c–6f and Fig. S14. It is observed that there is almost no any change in valence state of Co and material morphology before and after use, which further indicates long-term stability of CAO@AO-2.

3.6. Upgrading CAO@AO catalysts for PMS activation and MNZ degradation

Through the "hydrothermal–Co^{2+} adsorption–calcination" procedure, we successfully fabricated CAO@AO catalysts and confirmed their remarkable catalytic performance in activating PMS for degradation of MNZ and other refractory organic pollutants. Motivated by these results, further efforts were made to upgrade CAO@AO catalysts by replacing a part of Co species with the foreign metal M (M = Fe, Mn, or Cu). Reasons for replacing Co with M is based on the following considerations: 1) partial substitution of cheap and low-toxicity M in the CAO@AO will reduce the use of cobalt, which is of economic and environmental significance; and 2) the presence of suitable M might be beneficial in promoting the catalytic efficiency of CAO@AO [12]. For these purposes, a series of M-substituted CAO@AO catalysts (M(*y*%)-CAO@AO, M = Fe, Mn, or Cu; *y*% represents the molar percentage of M/(M+Co)) were synthesized according to the similar procedure for CAO@AO-2, and the total amount of M and Co in each M-substituted CAO@AO catalyst was equivalent to the Co content in the CAO@AO-2. The consents of Co, Al and M in M(*y*%)-CAO@AO were determined by ICP–OES, and the results are summarized in Table S4-S6. Then, the as-synthesized M-substituted CAO@AO catalysts were characterized by multiple techniques including SEM, XRD and ICP–OES, confirming that they have similar physicochemical features to that of CAO@AO-2 except for the difference in

content of M and Co (Fig. S15-S20). These results indicate that our synthetic method has merits of being extended, which makes it possible to obtain advanced versatile catalysts for potential applications in diverse areas.

Fig. 7a, c, and e show the MNZ degradation in M(*y*%)-CAO@AO/PMS and CAO@AO-2/PMS systems. Interestingly, although single use of M (Mn, Fe, or Cu) as active sites has a very weak or even negligible ability for MNZ removal, the M(*y*%)-CAO@AO/PMS catalysts with coexistence of M and Co show high catalytic degradation efficiencies (Fig. 7a, c, and e). In particular, an appropriate amount of M in the catalysts (i.e., $y\% \leq 20\%$ for Fe, $y\% \leq 40\%$ for Mn, and $y\% \leq 20\%$ for Cu) reaches ultrahigh catalytic efficiencies that are even superior to that of CAO@AO-2. According to the literature and our previous studies, the enhanced catalytic performance should be due to the promoting effect of Fe, Mn, and Cu [76,77]. The possible promoting reaction are listed in Table S7. To better visualize the catalytic performance of M(*y*%)-CAO@AO/PMS, their TOF values were also calculated, and the results are shown in Fig. 7b, d, and f. It can be clearly seen that the presence of M in the M(*y*%)-CAO@AO/PMS is indeed capable of enhancing the catalytic ability. With the increment of M percentage, the TOF values increase and reach their plateaus when the *y*% values of Fe, Mn, and Cu exceed 40%, 50%, and 40%, respectively (Fig. 7b, d, and f). Particularly, the plateau value (5.82 min^{-1}) of TOF for Mn(*y*%)-CAO@AO/PMS ($y\% \geq 40\%$) is 3.2 times higher than that (1.83 min^{-1}) of CAO@AO-2.

Besides, it is also observed that no cobalt leaching is observed in all

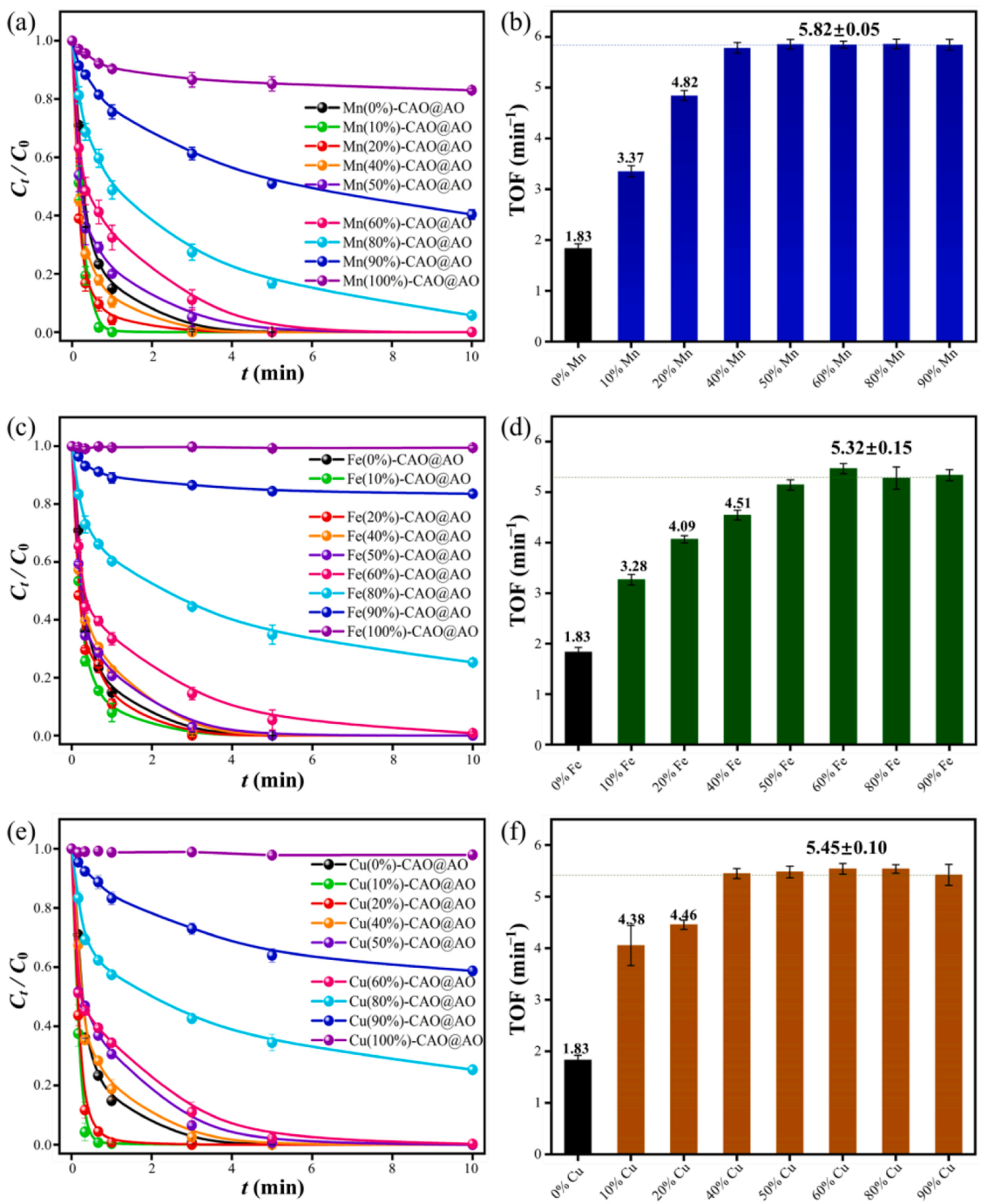

Fig. 7. Catalytic degradation behaviors and TOF values of Mn(*y*%)-CAO@AO (a and b), Fe(*y*%)-CAO@AO (c and d), and Cu(*y*%)-CAO@AO (e and f).

cases, which should be due to the pH buffering function of the catalysts (Fig. S21). These results indicate that the incorporation of suitable foreign metals in an appropriate level is a promising way to maximize the catalytic performance of CAO@AO catalysts.

In order to better meet the requirements of practical applications, the highly-active yet durable Mn(40%)-CAO@AO was in situ formed on the surface of granular porous alumina (GPA, ca. 1.5–2.5 mm) to obtain a large-sized catalyst (Mn(40%)-CAO@AO/GPA). It is worth noting that the synthesis of Mn(40%)-CAO@AO/GPA is rather simple, as described in Fig. 8a (The detail is described in Text S1). Using this process, we have obtained sub-kilogram quantities of Mn(40%)-CAO@AO/GPA (Fig. 8a). From Fig. 8b, it can be observed, the surface of GPA skeleton is composed of hierarchical nanosheets (Fig. S22), which should be assigned to Mn(40%)-CAO@AO. The EDS mapping results in Fig. 8c show that the Al, O, Co, and Mn elements are uniformly distributed on the Mn(40%)-CAO@AO/GPA catalyst. Fig. 8d shows the high-resolution spectra of Co and Mn elements on the surface of the material, where the Co 2p orbital is highly similar to that of the CAO@AO-2 material, indicating that the introduction of Mn does not change the form of Co. The Mn 2p orbital can split into two distinctive peaks at binding energies of 642.8 and 654.4 eV, corresponding to the Mn $2p_{3/2}$ and Mn $2p_{1/2}$ states, respectively, and the spacing between the two characteristic peaks is 11.6 eV. These results confirm that the oxidation valence state of Mn in the Mn(40%)-CAO@AO/GPA is + 2, which might refelect the formation of $Co_{1-x}Mn_xAl_2O_4$ [78]. This is further supported by the presence of the characteristic satellite peak of Mn^{2+} at the binding energy of 647.4 eV [79]. Fig. S23 shows the XRD patterns of GPA, hydrothermal product, and Mn(40%)-CAO@AO/GPA. With use of a column reactor packed with 10 g of Mn(40%)-CAO@AO/GPA as the fixed bed, a continuous-flow experiment was carried out (Fig. 8e). Fig. 8f show the time-dependent removal of MNZ by this continuous-flow column reactor. It can be clearly seen that a complete removal of MNZ with volume of up to 1000 mL can be achieved and cobalt leaching can be avoided within 90 min (Fig. S24), which demonstrates that the possibility of the Mn(40%)-CAO@AO/GPA catalyst for directly treating practical wastewater. Furthermore, if multiple column reactors are

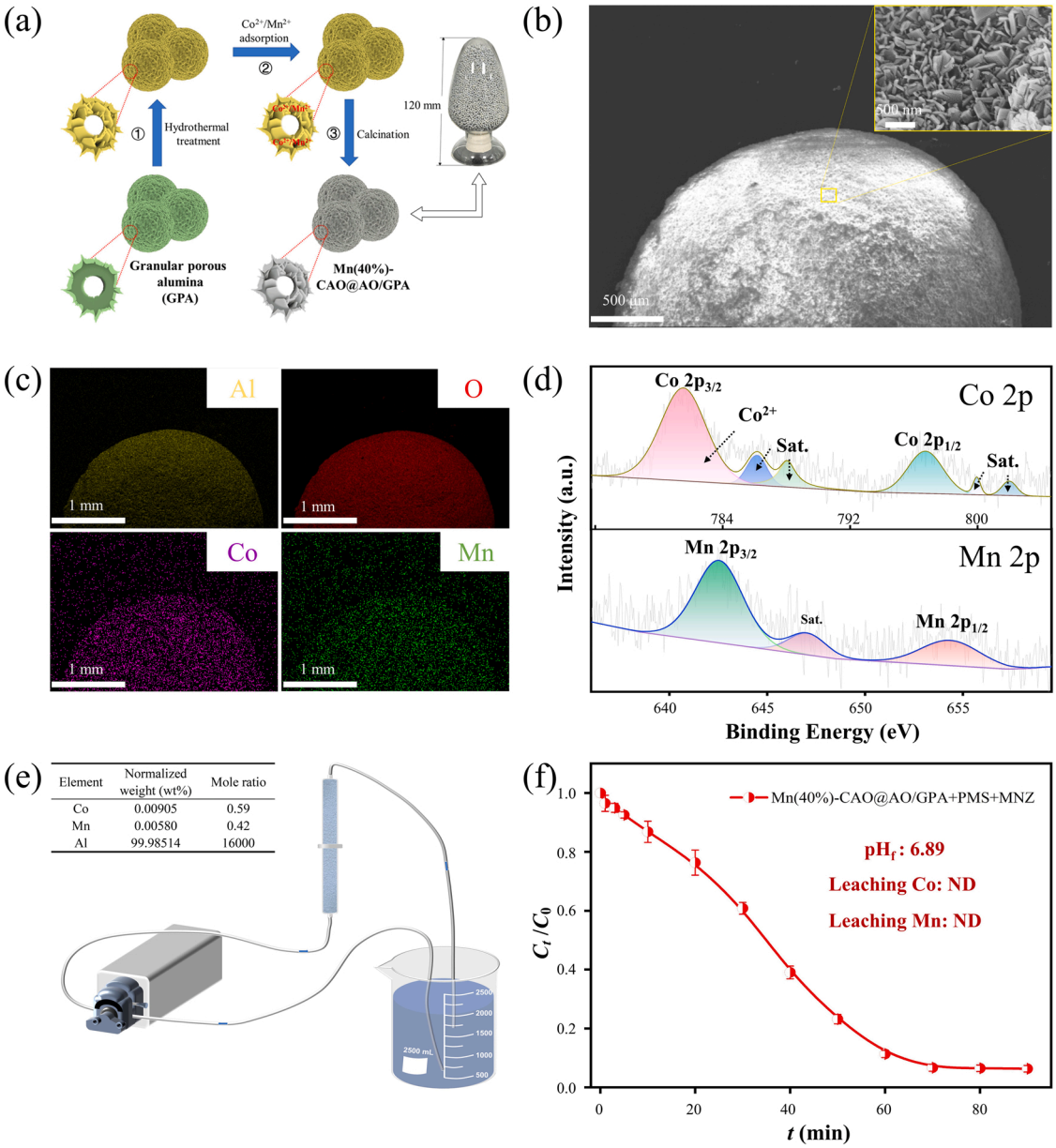

Fig. 8. Preparation process of (a), SEM images (b), EDS mapping characterization (c) of Mn(40%)-CAO@AO/GPA; high-resolution XPS spectra of Co 2p and Mn 2p (d); schematic diagram of flow-through treatment for catalytic degradation of MNZ (e); results of flow-through treatment of MNZ by Mn(40%)-CAO@AO/GPA (f).

connected in series, it should be available to efficiently eliminate organic pollutants on a large scale.

4. Conclusions

In summary, we reported the facile synthesis of Co−Al oxide clusters-embedded γ-Al_2O_3 nanosheets (CAO@AO) catalysts and demonstrated their promising applications in leaching-free and high-efficiency activation of PMS for removal of antibiotics and other pollutants. Owing to the unique interfacial pH-buffering property and Al–OH-promoted effect, the as-prepared CAO@AO was highly active and pretty stable without any cobalt leaching during PMS activation, enabling complete and ultrafast removal of MNZ and impressive reusability during the cyclic use. Moreover, the reaction kinetics, degradation pathway, and catalytic mechanism were also investigated and elucidated. Besides, the technical upgradation of CAO@AO-mediated PMS oxidation was further achieved through tunning of active component and immobilization on granulated support. This novel concept of interfacial pH-buffering solid cobalt-based catalyst provides a simple, efficient, and environmentally benign way for PMS activation to degrade various refractory organic pollutants.

CRediT authorship contribution statement

Ding Liu: Investigation, Methodology, Writing – original draft preparation; **Zhenkun Su**: Investigation, Data curation; **Bo Han**: Software, Validation; **Kaisheng Xia**: Funding acquisition; **Chenggang Zhou**: Supervision; **Qiang Gao**: Conceptualization, Writing – review & editing, Project administration.

Declaration of Competing Interest

The authors declare that they have no known competing financial interests or personal relationships that could have appeared to influence the work reported in this paper.

Data Availability

Data will be made available on request.

Acknowledgements

The authors gratefully acknowledge financial support from National Natural Science Foundation of China (No. 21975228), the Open Fund of Guangdong Provincial Key Laboratory of Advance Energy Storage Materials (No. AESM201815), and the Open Fund of State Key Laboratory of Materials Processing and Die and Mould Technology, Huazhong University of Science and Technology (No. P2020-011).

Appendix A. Supporting information

Supplementary data associated with this article can be found in the online version at doi:10.1016/j.apcatb.2023.122555.

References

[1] B. Wang, Y. Wang, A comprehensive review on persulfate activation treatment of wastewater, Sci. Total. Environ. 831 (2022), 154906.
[2] C. Cheng, Q. Liang, M. Yan, Z. Liu, Q. He, T. Wu, S. Luo, Y. Pan, C. Zhao, Y. Liu, Advances in preparation, mechanism and applications of graphene quantum dots/semiconductor composite photocatalysts: a review, J. Hazard. Mater. 424 (2022), 127721.
[3] C. Zhao, B. Shao, M. Yan, Z. Liu, Q. Liang, Q. He, T. Wu, Y. Liu, Y. Pan, J. Huang, J. Wang, J. Liang, L. Tang, Activation of peroxymonosulfate by biochar-based catalysts and applications in the degradation of organic contaminants: a review, Chem. Eng. J. 416 (2021), 128829.
[4] V. Parvulescu, F. Epron, H. Garcia, P. Granger, Recent progress and prospects in catalytic water treatment, Chem. Rev. 122 (2022) 2981–3121.
[5] B. Li, Y. Wang, L. Zhang, H. Xu, Enhancement strategies for efficient activation of persulfate by heterogeneous cobalt-containing catalysts: A review, Chemosphere 291 (2022), 132954.
[6] J. Hou, X. He, S. Zhang, J. Yu, M. Feng, X. Li, Recent advances in cobalt-activated sulfate radical-based advanced oxidation processes for water remediation: a review, Sci. Total. Environ. 770 (2021), 145311.
[7] Z. Liu, X. Ren, X. Duan, A. Sarmah, X. Zhao, Remediation of environmentally persistent organic pollutants (POPs) by persulfates oxidation system (PS): a review, Sci. Total. Environ. (2022), 160818.
[8] J. Sun, T. Wu, Z. Liu, B. Shao, Q. Liang, Q. He, S. Luo, Y. Pan, C. Zhao, D. Huang, Peroxymonosulfate activation induced by spinel ferrite nanoparticles and their nanocomposites for organic pollutants removal: a review, J. Clean. Prod. 346 (2022), 131143.
[9] W. Oh, V. Chang, Z. Hu, R. Goei, T. Lim, Enhancing the catalytic activity of g-C_3N_4 through Me doping (Me = Cu, Co and Fe) for selective sulfathiazole degradation via redox-based advanced oxidation process, Chem. Eng. J. 323 (2017) 260–269.
[10] M. He, Q. Liang, L. Tang, Z. Liu, B. Shao, Q. He, T. Wu, S. Luo, Y. Pan, C. Zhao, C. Niu, Y. Hu, Advances of covalent organic frameworks based on magnetism: Classification, synthesis, properties, applications, Coord. Chem. Rev. 449 (2021), 214219.
[11] Q. Liang, X. Liu, B. Shao, L. Tang, Z. Liu, W. Zhang, S. Gong, Y. Liu, Q. He, T. Wu, Y. Pan, S. Tong, Construction of fish-scale tubular carbon nitride-based heterojunction with boosting charge separation in photocatalytic tetracycline degradation and H_2O_2 production, Chem. Eng. J. 426 (2021), 130831.
[12] J. Li, M. Xu, G. Yao, B. Lai, Enhancement of the degradation of atrazine through $CoFe_2O_4$ activated peroxymonosulfate (PMS) process: Kinetic, degradation intermediates, and toxicity evaluation, Chem. Eng. J. 348 (2018) 1012–1024.
[13] L. Long, L. Su, W. Hu, S. Deng, C. Chen, F. Shen, M. Xu, G. Huang, G. Yang, Micro-mechanism of multi-pathway activation peroxymonosulfate by copper-doped cobalt silicate: The dual role of copper, Appl. Catal. B Environ. 309 (2022), 121276.
[14] J. Deng, C. Ya, Y. Ge, Y. Cheng, Y. Chen, M. Xu, H. Wang, Activation of peroxymonosulfate by metal (Fe, Mn, Cu and Ni) doping ordered mesoporous Co_3O_4 for the degradation of enrofloxacin, RSC Adv. 8 (2018) 2338–2349.
[15] H. Li, Q. Gao, G. Wang, B. Han, K. Xia, C. Zhou, Architecturing $CoTiO_3$ overlayer on nanosheets-assembled hierarchical TiO_2 nanospheres as a highly active and robust catalyst for peroxymonosulfate activation and metronidazole degradation, Chem. Eng. J. 392 (2020), 123819.
[16] H. Li, Q. Gao, G. Wang, B. Han, K. Xia, J. Wu, C. Zhou, J. Dong, Postsynthetic incorporation of catalytically inert Al into Co_3O_4 for peroxymonosulfate activation and insight into the boosted catalytic performance, Chem. Eng. J. 426 (2021), 131292.
[17] C. Chen, L. Liu, Y. Li, W. Li, L. Zhou, Y. Lan, Y. Li, Insight into heterogeneous catalytic degradation of sulfamethazine by peroxymonosulfate activated with $CuCo_2O_4$ derived from bimetallic oxalate, Chem. Eng. J. 384 (2020), 123257.
[18] X. Duan, C. Su, J. Miao, Y. Zhong, Z. Shao, S. Wang, H. Sun, Insights into perovskite-catalyzed peroxymonosulfate activation: Maneuverable cobalt sites for promoted evolution of sulfate radicals, Appl. Catal. B Environ. 220 (2018) 626–634.
[19] S. Hammouda, F. Zhao, Z. Safaei, V. Srivastava, D. Ramasamy, S. Iftekhar, S. kalliola, M. Sillanpää, Degradation and mineralization of phenol in aqueous medium by heterogeneous monopersulfate activation on nanostructured cobalt based-perovskite catalysts $ACoO_3$ (A = La, Ba, Sr and Ce): Characterization, kinetics and mechanism study, Appl. Catal. B Environ. 215 (2017) 60–73.
[20] G. Anipsitakis, E. Stathatos, D. Dionysiou, Heterogeneous activation of oxone using Co_3O_4, J. Phys. Chem. B 109 (2005) 13052–13055.
[21] P. Hu, M. Long, Cobalt-catalyzed sulfate radical-based advanced oxidation: A review on heterogeneous catalysts and applications, Appl. Catal. B Environ. 181 (2016) 103–117.
[22] Y. Pi, H. Gao, Y. Cao, R. Cao, Y. Wang, J. Sun, Cobalt ferrite supported on carbon nitride matrix prepared using waste battery materials as a peroxymonosulfate activator for the degradation of levofloxacin hydrochloride, Chem. Eng. J. 379 (2020), 122377.
[23] R. Zhang, Y. Wan, J. Peng, G. Yao, Y. Zhang, B. Lai, Efficient degradation of atrazine by $LaCoO_3/Al_2O_3$ catalyzed peroxymonosulfate: Performance, degradation intermediates and mechanism, Chem. Eng. J. 372 (2019) 796–808.
[24] H. Xu, D. Wang, J. Ma, T. Zhang, X. Lu, Z. Chen, A superior active and stable spinel sulfide for catalytic peroxymonosulfate oxidation of bisphenol S, Appl. Catal. B Environ. 238 (2018) 557–567.
[25] Y. Wang, S. Zhao, W. Fan, Y. Tian, X. Zhao, The synthesis of novel Co–Al_2O_3 nanofibrous membranes with efficient activation of peroxymonosulfate for bisphenol A degradation, Environ. Sci. Nano 5 (2018) 1933–1942.
[26] S. Lambert, A. Davy, Water quality as a threat to aquatic plants: discriminating between the effects of nitrate, phosphate, boron and heavy metals on charophytes, New Phytol. 189 (2011) 1051–1059.
[27] K. Szymanek, R. Charmas, W. Piasecki, Investigations of mechanism of Ca^{2+} adsorption on silica and alumina based on Ca-ISE monitoring, potentiometric titration, electrokinetic measurements and surface complexation modeling, Adsorption 27 (2020) 105–115.
[28] M. Wawrzkiewicz, M. Wiśniewska, A. Wołowicz, V. Gun'ko, V. Zarko, Mixed silica-alumina oxide as sorbent for dyes and metal ions removal from aqueous solutions and wastewaters, Microporous Mesoporous Mater. 250 (2017) 128–147.
[29] X. Yang, Q. Li, E. Lu, Z. Wang, X. Gong, Z. Yu, Y. Guo, L. Wang, Y. Guo, W. Zhan, J. Zhang, S. Dai, Taming the stability of Pd active phases through a compartmentalizing strategy toward nanostructured catalyst supports, Nat. Commun. 10 (2019) 1611.

[30] J. Sun, Y. Wang, H. Zou, X. Guo, Z. Wang, Ni catalysts supported on nanosheet and nanoplate γ-Al_2O_3 for carbon dioxide methanation, J. Energy Chem. 29 (2019) 3–7.
[31] A. Quindimil, M. Bacariza, J. González, C. Henriques, J. González, Enhancing the CO_2 methanation activity of γ-Al_2O_3 supported mono- and bi-metallic catalysts prepared by glycerol assisted impregnation, Appl. Catal. B Environ. 296 (2021), 120322.
[32] N. Merle, T. Tabassum, S. Scott, A. Motta, K. Szeto, M. Taoufik, R. Gauvin, L. Delevoye, High-field NMR, reactivity, and DFT modeling reveal the gamma-Al_2O_3 surface hydroxyl network, Angew. Chem. Int. Ed. Engl. 61 (2022), e202207316.
[33] B. Zhang, S. Xiang, A. Frenkel, I. Wachs, Molecular design of supported MoO_x catalysts with surface TaO_x promotion for olefin metathesis, ACS Catal. 12 (2022) 3226–3237.
[34] S. Liu, X. Liang, J. Zhang, B. Chen, Temperature sensitive synthesis of γ-Al_2O_3 support with different morphologies for CoMo/γ-Al_2O_3 catalysts for hydrodesulfurization of thiophene and 4,6-dimethyldibenzothiophene, Catal. Sci. Technol. 7 (2017) 466–480.
[35] F. Wang, J. Ma, S. Xin, Q. Wang, J. Xu, C. Zhang, H. He, X. Cheng, Resolving the puzzle of single-atom silver dispersion on nanosized gamma-Al_2O_3 surface for high catalytic performance, Nat. Commun. 11 (2020) 529.
[36] S. Vierck, C. Leclerc, A temperature programmed desorption study of non-thermal plasma modified γ-Al_2O_3, Adv. Powder Technol. 28 (2017) 1792–1796.
[37] J. Park, J. Regalbuto, A simple, accurate determination of oxide PZC and the strong buffering effect of oxide surfaces at incipient wetness, J. Colloid Interface Sci. 175 (1995) 239–252.
[38] M. Zhu, J. Yang, X. Duan, D. Zhang, S. Wang, B. Yuan, M. Fu, Interfacial $CoAl_2O_4$ from ZIF-67@γ-Al_2O_3 pellets toward catalytic activation of peroxymonosulfate for metronidazole removal, Chem. Eng. J. 397 (2020), 125339.
[39] M. Zhu, J. Yang, X. Duan, S. Wang, D. Sun, B. Yuan, M. Fu, Engineered Co_2AlO_4/$CoAl_2O_4$@Al_2O_3 monolithic catalysts for peroxymonosulfate activation: Co^{3+}/Co^{2+} and $O_{Defect}/O_{Lattice}$ ratios dependence and mechanism, Chem. Eng. J. 409 (2021), 128162.
[40] W. Huang, G. Liu, X. Li, T. Qi, Q. Zhou, Z. Peng, Synthesis of mesoporous γ-Al_2O_3 with hydrangea-like by the ethanol-thermal method, Mater. Lett. 277 (2020), 128361.
[41] O. Al'myasheva, E. Korytkova, A. Maslov, V. Gusarov, Preparation of nanocrystalline alumina under hydrothermal conditions, Inorg. Mater. 41 (2005) 540–547.
[42] E. Genty, J. Brunet, R. Pequeux, S. Capelle, S. Siffert, R. Cousin, Effect of Ce substituted hydrotalcite-derived mixed oxides on total catalytic oxidation of air pollutant, Mater. Toda Proc. 3 (2016) 277–281.
[43] Y. Dai, J. Gu, S. Tian, Y. Wu, J. Chen, F. Li, Y. Du, L. Peng, W. Ding, Y. Yang, γ-Al_2O_3 sheet-stabilized isolate Co^{2+} for catalytic propane dehydrogenation, J. Catal. 381 (2020) 482–492.
[44] A. Dandapat, G. De, Host-mediated synthesis of cobalt aluminate/gamma-alumina nanoflakes: a dispersible composite pigment with high catalytic activities, ACS Appl. Mater. Interfaces 4 (2012) 228–234.
[45] C. Maurizio, N. El Habra, G. Rossetto, M. Merlini, E. Cattaruzza, L. Pandolfo, M. Casarin, XAS and GIXRD study of Co sites in $CoAl_2O_4$ layers grown by MOCVD, Chem. Mater. 22 (2010) 1933–1942.
[46] C. Álvarez, J. Reinosa, A. Campo, J. Fernández, 2D particles forming a nanostructured shell: A step forward cool NIR reflectivity for $CoAl_2O_4$ pigments, Dyes Pigm. 137 (2017) 1–11.
[47] J. Wang, J. Jiang, X. Wang, S. Liu, X. Shen, X. Cao, Y. Sun, L. Dong, X. Meng, A. Ragauskas, Y. Wang, Polyethylene upcycling to fuels: narrowing the carbon number distribution in n-alkanes by tandem hydropyrolysis/hydrocracking, Chem. Eng. J. 444 (2022), 136360.
[48] S. Mo, Q. Zhang, Q. Ren, J. Xiong, M. Zhang, Z. Feng, D. Yan, M. Fu, J. Wu, L. Chen, D. Ye, Leaf-like Co-ZIF-L derivatives embedded on Co_2AlO_4/Ni foam from hydrotalcites as monolithic catalysts for toluene abatement, J. Hazard. Mater. 364 (2019) 571–580.
[49] Y. Bao, W. Oh, T. Lim, R. Wang, R. Webster, X. Hu, Surface-nucleated heterogeneous growth of zeolitic imidazolate framework – A unique precursor towards catalytic ceramic membranes: Synthesis, characterization and organics degradation, Chem. Eng. J. 353 (2018) 69–79.
[50] J. Bao, X. Zhang, B. Fan, J. Zhang, M. Zhou, W. Yang, X. Hu, H. Wang, B. Pan, Y. Xie, Ultrathin spinel-structured nanosheets rich in oxygen deficiencies for enhanced electrocatalytic water oxidation, Angew. Chem. Int. Ed. Engl. 54 (2015) 7399–7404.
[51] D. Chvedov, S. Ostap, T. Le, Surface properties of red mud particles from potentiometric titration, Colloid Surf. A. 182 (2001) 131–141.
[52] G. Di, F. Maleki, G. Pacchioni, pH dependence of MgO, TiO_2, and γ-Al_2O_3 surface chemistry from first principles, J. Phys. Chem. C. 126 (2022) 10216–10223.
[53] J. Ji, X. Yao, J. Gao, W. Lu, W. Wang, D. Chu, Effect of surfactants and pH values on stability of γ-Al_2O_3 nanofluids, Chem. Phys. Lett. 781 (2021), 138996.
[54] L. Long, L. Su, W. Hu, S. Deng, C. Chen, F. Shen, M. Xu, G. Huang, G. Yang, Micro-mechanism of multi-pathway activation peroxymonosulfate by copper-doped cobalt silicate: The dual role of copper, Appl. Catal. B Environ. 309 (2022), 121276.
[55] J. Noh, J. Schwarz, Estimation of the point of zero charge of simple oxides by mass titration, J. Colloid Interface Sci. 130 (1988) 157–164.
[56] Y. Shen, W. Liu, K. Lin, H. Pan, B. Darvell, S. Peng, C. Wen, L. Deng, W. Lu, J. Chang, Interfacial pH: a critical factor for osteoporotic bone regeneration, Langmuir 27 (2011) 2701–2708.
[57] T. Wu, Q. He, Z. Liu, B. Shao, Q. Liang, Y. Pan, J. Huang, Z. Peng, Y. Liu, C. Zhao, X. Yuan, L. Tang, S. Gong, Tube wall delamination engineering induces photogenerated carrier separation to achieve photocatalytic performance improvement of tubular g-C_3N_4, J. Hazard. Mater. 424 (2022), 127177.
[58] P. Zhang, L. Sun, H. Wang, J. Cui, J. Hao, Surfactant-assistant atmospheric acid leaching of laterite ore for the improvement of leaching efficiency of nickel and cobalt, J. Clean. Prod. 228 (2019) 1–7.
[59] P. Shi, R. Su, F. Wan, M. Zhu, D. Li, S. Xu, Co_3O_4 nanocrystals on graphene oxide as a synergistic catalyst for degradation of Orange II in water by advanced oxidation technology based on sulfate radicals, Appl. Catal. B Environ. 123–124 (2012) 265–272.
[60] B. Shao, Z. Liu, G. Zeng, Y. Liu, Q. Liang, Q. He, T. Wu, Y. Pan, J. Huang, Z. Peng, S. Luo, C. Liang, X. Liu, S. Tong, J. Liang, Synthesis of 2D/2D CoAl-LDHs/$Ti_3C_2T_x$ Schottky-junction with enhanced interfacial charge transfer and visible-light photocatalytic performance, Appl. Catal. B Environ. 286 (2021), 119867.
[61] H. Wang, Q. Gao, H. Li, B. Han, K. Xia, C. Zhou, One-pot synthesis of a novel hierarchical Co(II)-doped TiO_2 nanostructure: Toward highly active and durable catalyst of peroxymonosulfate activation for degradation of antibiotics and other organic pollutants, Chem. Eng. J. 368 (2019) 377–389.
[62] S. Hammouda, F. Zhao, Z. Safaei, D. Ramasamy, B. Doshi, M. Sillanpää, Sulfate radical-mediated degradation and mineralization of bisphenol F in neutral medium by the novel magnetic Sr_2CoFeO_6 double perovskite oxide catalyzed peroxymonosulfate: Influence of co-existing chemicals and UV irradiation, Appl. Catal. B Environ. 233 (2018) 99–111.
[63] L. Hu, G. Zhang, M. Liu, Q. Wang, P. Wang, Enhanced degradation of Bisphenol A (BPA) by peroxymonosulfate with Co_3O_4-Bi_2O_3 catalyst activation: Effects of pH, inorganic anions, and water matrix, Chem. Eng. J. 338 (2018) 300–310.
[64] Y. Liu, R. Luo, Y. Li, J. Qi, C. Wang, J. Li, X. Sun, L. Wang, Sandwich-like Co_3O_4/MXene composite with enhanced catalytic performance for Bisphenol A degradation, Chem. l Eng. J. 347 (2018) 731–740.
[65] Y. Pan, X. Liu, W. Zhang, B. Shao, Z. Liu, Q. Liang, T. Wu, Q. He, J. Huang, Z. Peng, Y. Liu, C. Zhao, Bifunctional template-mediated synthesis of porous ordered g-C_3N_4 decorated with potassium and cyano groups for effective photocatalytic H_2O_2 evolution from dual-electron O_2 reduction, Chem. Eng. J. 427 (2022), 132032.
[66] D. Santos, O. Soares, J. Figueiredo, O. Sanz, M. Montes, M. Pereira, Preparation of ceramic and metallic monoliths coated with cryptomelane as catalysts for VOC abatement, Chem. Eng. J. 382 (2020), 122923.
[67] T. Wu, Z. Liu, B. Shao, Q. Liang, Q. He, Y. Pan, X. Zhang, Y. Liu, J. Sun, S. Gong, Hydrogen peroxide-impregnated supramolecular precursors synthesize mesoporous-rich ant nest-like filled tubular g-C_3N_4 for effective photocatalytic removal of pollutants, Chem. Eng. J. 447 (2022), 137332.
[68] X. Zhang, S. Tong, D. Huang, Z. Liu, B. Shao, Q. Liang, T. Wu, Y. Pan, J. Huang, Y. Liu, M. Cheng, M. Chen, Recent advances of Zr based metal organic frameworks photocatalysis: Energy production and environmental remediation, Coordin. Chem. Rev. 448 (2021), 214177.
[69] M. Zhu, D. Guan, Z. Hu, H. Lin, C. Chen, H. Sheu, S. Wang, J. Zhou, W. Zhou, Z. Shao, Synergistic effects in ordered Co oxides for boosting catalytic activity in advanced oxidation processes, Appl. Catal. B Environ. 297 (2021), 120463.
[70] H. Dong, J. Chen, L. Feng, W. Zhang, X. Guan, T. Strathmann, Degradation of organic contaminants through activating bisulfite by cerium(IV): A sulfate radical-predominant oxidation process, Chem. Eng. J. 357 (2019) 328–336.
[71] J. Liang, X. Duan, X. Xu, K. Chen, Y. Zhang, L. Zhao, H. Qiu, S. Wang, X. Cao, Persulfate oxidation of sulfamethoxazole by magnetic iron-char composites via nonradical pathways: Fe(IV) versus surface-mediated electron transfer, Environ. Sci. Technol. 55 (2021) 10077–10086.
[72] U. Ushani, X. Lu, J. Wang, Z. Zhang, J. Dai, Y. Tan, S. Wang, W. Li, C. Niu, T. Cai, N. Wang, G. Zhen, Sulfate radicals-based advanced oxidation technology in various environmental remediation: A state-of-the–art review, Chem. Eng. J. 402 (2020), 126232.
[73] J. Yang, D. Zeng, J. Li, L. Dong, W. Ong, Y. He, A highly efficient Fenton-like catalyst based on isolated diatomic Fe-Co anchored on N-doped porous carbon, Chem. Eng. J. 404 (2021), 126376.
[74] R. Yuan, L. Hu, P. Yu, Z. Wang, H. Wang, J. Fang, Co_3O_4 nanocrystals/3D nitrogen-doped graphene aerogel: A synergistic hybrid for peroxymonosulfate activation toward the degradation of organic pollutants, Chemosphere 210 (2018) 877–888.
[75] F. Wang, Y. Lai, Q. Fang, Z. Li, P. Ou, P. Wu, Y. Duan, Z. Chen, S. Li, Y. Zhang, Facile fabricate of novel Co(OH)F@MXenes catalysts and their catalytic activity on bisphenol A by peroxymonosulfate activation: The reaction kinetics and mechanism, Appl. Catal. B Environ. 262 (2020), 118099.
[76] Q. Pan, Q. Gao, G. Gao, M. Liu, B. Han, K. Xia, C. Zhou, Composition-engineered $LaCoO_3$-based monolithic catalysts for easily operational and robust peroxymonosulfate activation, Chem. Eng. J. 424 (2021), 130574.
[77] M. Xu, J. Li, Y. Yan, X. Zhao, J. Yan, Y. Zhang, B. Lai, X. Chen, L. Song, Catalytic degradation of sulfamethoxazole through peroxymonosulfate activated with expanded graphite loaded $CoFe_2O_4$ particles, Chem. Eng. J. 369 (2019) 403–413.
[78] W. Zhang, W. Zhou, J. Wright, Y. Kim, D. Liu, X. Xiao, Mn-doped TiO_2 nanosheet-based spheres as anode materials for lithium-ion batteries with high performance at elevated temperatures, ACS Appl. Mater. Interfaces 6 (2014) 7292–7300.
[79] H.T. Li, Q. Gao, B. Han, Z.H. Ren, K.S. Xia, C.G. Zhou, Partial-redox-promoted mn cycling of Mn(II)-doped heterogeneous catalyst for efficient H_2O_2-mediated oxidation, ACS Appl. Mater. Interfaces 9 (2017) 371–380.